

UNIVERSITY OF PISA

FACULTY OF MATHEMATICAL, PHYSICAL AND NATURAL SCIENCES

THESIS IN PHYSICS

---

**Experimental characterization of  
blackbody induced transitions in  
high-lying Rydberg states**

---

*Author:*

Matteo CECCANTI

*Supervisor:*

Dr. Oliver MORSCH



18/07/2019

*Alla mia famiglia...*

# Ringraziamenti

Finalmente mi trovo a scrivere queste ultime pagine della tesi, pagine molto importanti, in cui voglio esprimere la mia gratitudine verso tutte quelle persone che hanno contribuito al mio sviluppo personale e professionale.

Innanzitutto voglio ringraziare il Prof. Oliver Morsch per i preziosi consigli e per la pazienza dimostrata in questo lungo periodo, grazie ai quali ho imparato a muovermi in autonomia in un laboratorio di Fisica. Inoltre voglio ringraziarlo per le lunghe chiacchierate di fronte a un caffè che hanno reso questo periodo meno pesante e mi hanno fatto sentire qualcosa di più di un semplice studente.

Ringrazio tutto il gruppo di ricerca: Alessandro, Lucia, Donatella per le discussioni che mi hanno aiutato a sviluppare l'esperimento. Un ringraziamento particolare va a Matteo, che nonostante i suoi impegni e il suo carattere a volte scontroso, si è rivelato una delle persone più gentili e disponibili che ho mai conosciuto.

Un grande ringraziamento va al Chiarissimo Prof. Francesco Fuso, per avermi sempre parlato con modi garbati ed educati e per avermi costantemente rassicurato sull'esito della mia prova, dicendomi ogni giorno: "Tanto ti bocciano, preparati a ripetere i 5 anni".

Certamente devo ringraziare tutto il gruppo dei *più tosti*: per avermi sopportato in questi difficili 5 anni, per le incoscienti serate in piazza dei Cavalieri e per tutti quei pomeriggi passati a far finta di studiare, voi tutti siete uno dei motivi per cui ricorderò felicemente questo periodo di studi.

Ringrazio tutto il gruppo degli amici storici di Calcinaia, che, nonostante la mia vita mi abbia portato ad allontanarmi da loro, non hanno mai smesso di essere veri amici.

Tra tutte queste persone è doveroso fare un ringraziamento particolare ad Antonio, Niccolò e Simone, gli amici che negli ultimi anni hanno fortemente contribuito sia al mantenimento della mia sanità mentale (non ce l' hanno fatta ma almeno ci hanno provato), che al raggiungimento dei miei risultati. Non mi scorderò mai tutti quei viaggi verso Pisa ascoltando buona musica e le infinite giornate in Paci passate tra una pausa caffè e una pausa cicchino. Oltre a tutte queste persone, un immenso ringraziamento va a chi questo percorso lo ha

vissuto direttamente accanto a me, Sara. Voglio ringraziarla, in primis, per aver sopportato i miei noiosi discorsi da fisico, non voglio immaginare quanto pesante io possa essere stato. Soprattutto però, voglio ringraziarla per le tante esperienze che mi ha fatto vivere, percorrendo insieme quei passi che mi hanno fatto diventare la persona che sono adesso, dandomi sempre la forza di non mollare.

Infine, il più grande ringraziamento va alla mia famiglia: Mariarosa, Endrio e Filippo per avermi dato la possibilità di intraprendere questo percorso di studi, credendo in me anche quando nemmeno io ci credevo, per avermi insegnato ad affrontare le difficoltà sempre con un sorriso e per non aver mai smesso di darmi tutto il sostegno che potevano.

Sono veramente orgoglioso di tutte le persone che mi sono state vicine. Grazie di cuore.

# Contents

<b>1</b>	<b>Theoretical background</b>	<b>1</b>
1.1	Theoretical treatment of the Rydberg states lifetime . . . . .	2
1.1.1	Repopulation processes . . . . .	5
1.2	The blackbody radiation in a box . . . . .	6
1.2.1	The Purcell effect . . . . .	6
1.3	Interaction with DC electric fields: the Stark effect . . . . .	7
1.3.1	The quadratic Stark effect . . . . .	8
1.3.2	The linear Stark effect . . . . .	9
1.3.3	Ionisation thresholds . . . . .	9
1.4	Rydberg-Rydberg interactions . . . . .	10
1.5	Interaction with AC Electric fields: the dressed atom approach . . . . .	11
<b>2</b>	<b>Description of the experimental set-up</b>	<b>14</b>
2.1	Trapping and detecting systems . . . . .	14
2.1.1	The Magneto optical trap . . . . .	14
2.1.2	Detection system . . . . .	16
2.2	Excitation techniques . . . . .	18
2.2.1	Excitation laser set-up . . . . .	18
2.2.2	Microwaves set-up . . . . .	21
2.3	Stray electric field compensation . . . . .	25
2.4	Fabry-Pérot stabilisation . . . . .	27
<b>3</b>	<b>Measurement of the S, P and D Rydberg state lifetime</b>	<b>29</b>
3.1	Experimental conditions . . . . .	29
3.2	De-excitation techniques . . . . .	31
3.2.1	De-excitation for S-D states . . . . .	31
3.3	S-D states lifetime protocol . . . . .	32

3.3.1	Results and discussion for S states . . . . .	34
3.3.2	De-excitation for P states . . . . .	37
3.4	P states lifetime protocol . . . . .	38
3.4.1	Results and discussion for P states . . . . .	39
3.5	Result for D states . . . . .	42
3.6	Conclusions . . . . .	42
<b>4</b>	<b>Simulation of Rydberg dynamics</b>	<b>44</b>
4.1	ARC-Alkali Rydberg Calculator . . . . .	44
4.2	Lifetime simulation . . . . .	47
4.2.1	Approximations . . . . .	47
4.2.2	The core of the simulation program . . . . .	48
4.2.3	Result for S and P states and quality check . . . . .	49
4.2.4	Simulation of mixture excitation . . . . .	51
4.2.5	Simulation of inefficient de-excitation . . . . .	53
4.3	Comparison with theoretical predictions in literature . . . . .	55
4.4	Conclusion . . . . .	56
<b>5</b>	<b>Qualitative analysis of Blackbody spectrum in our apparatus</b>	<b>57</b>
5.1	Simple model for the expected deviation . . . . .	58
5.2	Toy model for the calculation of the blackbody spectrum . . . . .	61
5.3	Conclusion . . . . .	63
<b>6</b>	<b>Conclusion</b>	<b>64</b>
<b>A</b>	<b>Calculation of the three-photon Rabi frequency</b>	<b>66</b>
<b>B</b>	<b>Lifetime program</b>	<b>68</b>
B.1	Definition of the structure STATE . . . . .	68
B.2	Evolution of a state . . . . .	70
	<b>Bibliography</b>	<b>72</b>

# Introduction

The advent of quantum mechanics completely revolutionised the human understanding of nature. In the physics scenario of XX century most unsolvable problems of classical mechanics have been resolved but new, more complicated, questions raise. For example quantum many-body problems for which an analytical or computational description seems impossible without strong approximations. The problem in simulating a system of interacting quantum particles is that the physical elements of the computers used to simulate them behave classically, so that taking into account all the possible quantum many-body states requires an amount of memory impossible to achieve [1].

The question is, if such systems are composed by quantum particles, can we use a quantum system to simulate them? R. Feynman stated in 1981: "*Nature isn't classical, dammit, and if you want to make a simulation of nature, you'd better make it quantum mechanical, and by golly it's a wonderful problem, because it doesn't look so easy*". Nowadays this problem still doesn't look so easy, but much progress has been made since 1981; the development of laser technologies and cooling and trapping systems allows to have a good control on atomic quantum states and their further evolution. Buiding on those developments, the physical implementations of quantum simulators are now becoming a reality. Such a system has to be composed of quantum particles with strong controllable interactions and long lifetime. One particular physical system that has all the required properties is the Rydberg atom [2].

When an electron in an atom is excited to a Rydberg state, the resulting Rydberg atom exhibits peculiar properties such as a very large polarisability that implies strong interactions with external electromagnetic fields, but also significant dipole-dipole interactions with which various dynamics can be studied [3] and finally long lifetime that allows the implementation of processes of long duration.

A first step towards the realisation of a quantum simulator using Rydberg atoms is the experimental demonstration of their long lifetime, on the order of hundreds of microseconds, and the understanding of the conditions which cause alterations of this property. The strong coupling with external electromagnetic fields, combined with the small energy differences

between neighbouring levels make Rydberg states sensitive even to the blackbody radiation emitted by objects surrounding it, in spite of the weak intensity of such a radiation [4]. A Rydberg atom, in fact, has been proposed as an optimal sensor to study possible corrections to Planck's formula when the approximations necessary to derive it are not satisfied [5].

In the literature various experiments regarding the measurement of Rubidium Rydberg states lifetime with principal quantum number lower than 48 for S, P and D Rydberg states [6], [7],[8] are presented. Our aim is to increase the range of principal quantum numbers investigated.

In this thesis the experimental measurement of the lifetime of Rydberg states with principal quantum number up to 105 are reported for S, P and D angular momenta with a new hybrid technique that uses state-selective de-excitation combined with field ionisation. We demonstrate that our technique is limited principally by extremely small, stray electric fields, but, ideally, with a perfect compensation of such stray fields, our technique is limited only by the laser linewidth [9].

My work is the continuation of the PhD work of M. Archimi [10] and the thesis works of A. Greco[11] and L. Di Virgilio [12]. My personal contribution to the experiments is the realisation of the procedure for direct P-state excitation based on three-photon processes and the subsequent P-state de-excitation exploiting two-photon transitions. Furthermore I have designed and mounted the electrodes for the stray electric field compensation defining a protocol that allowed us to reduce the modulus of the residual electric field to about 17 mV/cm and consequently to work with principal quantum numbers up to 120. Finally I realised a numerical simulation of the evolution of a Rydberg state interacting with blackbody radiation obtaining the theoretical predictions with which our experimental data are compared.

In chapter 1 the theoretical treatment of a Rydberg state is presented, including the derivation of all the physical properties relevant to the investigated phenomena. In the first section the Rydberg atoms are introduced, defining the energy of a given excited state and the quantum number which identify it. After that I show the theoretical expressions for the lifetime of a Rydberg atom interacting with blackbody radiation presenting in the section a brief theoretical derivation of Planck's formula and discussing the validity of the approximations that lead to it. Moreover a discussion about interactions with an external field and between Rydberg atoms is reported, deriving for each property its approximate scaling law. Finally I briefly outline the dressed atom approach, which is useful to the description of atoms interacting with strong radiation fields.

In chapter 2 the experimental apparatus used to perform our experiments is described, in particular I present the basic concepts of our trapping and cooling system that is a *Magneto-*

*Optical Trap* (MOT) outlining the lasers preparation and their frequency stabilisation. Furthermore I present our detection system based on electric field ionisation, describing its characterisation and its limitations. After that, the light sources used for the two-photon and three-photon excitations are described. A brief presentation of our electric field compensation apparatus with the protocol used during the experiments completes the chapter together with a description of the Fabry-Pérot stabilisation scheme.

Chapter 3 starts with the description of the experimental conditions in which we work, taking care to describe the various parameters that can alter our results. Thereafter, the de-excitation scheme for S,P and D states is presented. The chapter proceeds with the presentation of the lifetime measurement protocols and the experimental results obtained for the S, P and D Rydberg states discussing them in terms of BBR enhanced transition rates. Chapter 4 analyses the simulations used to calculate theoretical predictions and to demonstrate the validity of our protocols.

Finally in chapter 5 a qualitative analysis of the experimental data is reported in terms of deviation from Planck's formula and a possible spectrum that fits our data is given.

# Chapter 1

## Theoretical background

Any element in the periodic table can, in principle, become a *Rydberg atom*. If an atom has at least one electron excited to a state with large principal quantum number, it is called Rydberg atom or, alternatively, it is excited to a Rydberg state.

The investigation on excited atomic states began in the XIX century with the experiments on spectral lines. One of the first empirical descriptions of the relation between atomic spectral wavelengths was made by Johannes Rydberg in 1888, who stated:

$$\frac{1}{\lambda} = \text{Ry} \left( \frac{1}{(n_1 - \delta_1)^2} - \frac{1}{(n_2 - \delta_2)^2} \right) \quad (1.1)$$

In this famous formula he related each observed wavelength ( $\lambda$ ) to integer values ( $n_1, n_2$ ) corrected by ( $\delta_1, \delta_2$ ) and the factor Ry, recognised as a universal constant, which could be used to describe the spectral lines of different atomic species.

More than one hundred years later, thanks to theoretical development of quantum mechanics, and in particular of atomic physics, equation (1.1) has been derived from fundamental properties, with the Rydberg constant defined as:

$$\text{Ry} = \frac{k_0^2 e^4 m_e}{4\pi \hbar^3 c} \left( 1 + \frac{m_e}{m_{nucleus}} \right)^{-1} = 10.9737 \left( 1 + \frac{m_e}{m_{nucleus}} \right)^{-1} \mu\text{m}^{-1} \quad (1.2)$$

where  $k_0 = \frac{1}{4\pi\epsilon_0}$  is the electrostatic constant,  $m_e$  is the electron mass and  $m_{nucleus}$  is the nuclear mass. This interpretation led us to understand that spectral lines are generated by the absorption or the emission of photons in quantum state transitions.

Considering alkali metals such as Rubidium, the species used in our experiments, the energy  $\epsilon_{nlj}$  of the outer electron is characterised by three quantum numbers:  $n$ , the principal quantum

number,  $l$ , the angular momentum and  $J$  the total angular momentum, in such a way:

$$\epsilon_{nlj} = -Ry \frac{1}{\left(n - \delta_l^{(X)}\right)^2} \quad (1.3)$$

here  $\delta_l^{(X)}$ , known as *quantum defect*, accounts for the presence of core electrons shells which do not entirely screen the nuclear charge. The quantum defect depends on the atomic species  $X$  and, to leading order, only on the angular momentum  $l$  [13].

$l$	$\delta_l$
0	3.13
1	2.64
2	1.35
3	0.016
$\geq 4$	0

Table 1.1:  $^{87}\text{Rb}$  quantum defects as a function of angular momentum

The behaviour of the outer electron is similar to the hydrogen one and from quantum defect theory is demonstrated that all the fundamental quantities describing its quantum state can be calculated by the substitution of  $n^* = (n - \delta_l^{(X)})$  for  $n$  in the formula for the hydrogen properties.

The properties of a Rydberg atom scale strongly the with principal quantum number [14], and for high-lying Rydberg states they take values that are vastly different from those of ground state atoms. Those extreme properties are the principal motivation for the interest in application in physical research. In the following sections I will highlight the physical properties involved in my thesis work, deriving their scaling laws with respect to principal quantum number.

## 1.1 Theoretical treatment of the Rydberg states lifetime

The lifetime of a Rydberg atom, completely isolated from every possible external perturbations, can be calculated as the inverse of the sum of all the possible spontaneous emission rates. For a specific transition ( $nlj \rightarrow n'l'j'$ ), the spontaneous emission rate is described by the Einstein A coefficient, that is defined as:

$$A_{nlj \rightarrow n'l'j'} = \frac{4e^2 \nu_{nlj \rightarrow n'l'j'}^3}{3(2\pi)^2 h c^3} \frac{\max(l, l')}{2l + 1} |\langle n'l' | \hat{r} | nl \rangle|^2 \quad (1.4)$$

in which  $\nu_{nlj \rightarrow n'l'j'} = (\epsilon_{nlj} - \epsilon_{n'l'j'})/h$  is the transition frequency between the two energy levels considered and  $\frac{\max(l,l')}{2l+1} |\langle n'l' | \hat{r} | nl \rangle|$  is the radial matrix element between such states. If we consider a state with energy  $\epsilon_{nlj}$ , a spontaneous decay process can happen only to states with lower energy. Calculating all the possible spontaneous emission rates, the lifetime of an excited state is easily calculated as:

$$\tau_n^{(isolated)} = \left( \sum_{\epsilon_{n'l'j'} < \epsilon_{nlj}} A_{nlj \rightarrow n'l'j'} \right)^{-1} \quad (1.5)$$

The factor  $\nu_{nlj \rightarrow n'l'j'}^3$  in (1.4) results in the fact that decay processes happen principally to low-lying states. The energy differences between an excited  $n > 20$  state and a low-lying state are approximately constant in  $n$ , as an example, considering two states with very different principal quantum numbers as  $40S$  and  $120S$  we have:  $\nu_{120S \rightarrow 5P} / \nu_{40S \rightarrow 5P} = 1.003$ . Therefore, for the evaluation of a scaling law, the transition frequency to low-lying states can be considered constant in  $n^*$ . By contrast, the dipole matrix elements to a low-lying state decrease with increasing principal quantum number, with a scaling law  $\langle 5P | r | nlj \rangle \propto n^{*-3/2}$ . Using these two simple assumptions, the resulting scaling law for the isolated lifetime can be approximated with:  $\tau_n^{(isolated)} \sim n^{*3}$  [5].

Nevertheless, in real experiments, the excited atoms are not completely isolated. The experimental apparatus surrounding them, being at a temperature  $T$ , emits radiation with a spectrum given by Planck's formula:  $u_\nu = \frac{8\pi\nu^2}{c^3} \frac{h\nu}{e^{h\nu/k_B T} - 1}$ . Contrary to dipole matrix elements to low-lying states, the dipole matrix elements between neighbouring levels are extremely large. Consequently, the thermal radiation, in spite of its very small intensity, it interacts with Rydberg states inducing transitions to other levels, both via absorption and stimulated emission. This fact results in a temperature dependence of the Rydberg states lifetime [15]. Excluding other possible perturbations we can refer to (1.5) as the lifetime at zero temperature:  $\tau_n^{(isolated)} = \tau_n(0K)$ .

The transition rates induced by blackbody radiation (BBR) can be calculated exploiting the Einstein B coefficients and the Planck's radiation intensity at the transition frequency:

$$\Gamma_{nlj \rightarrow n'l'j'}^{BBR} = B_{nlj \rightarrow n'l'j'} u_\nu(\nu_{nlj \rightarrow n'l'j'}, T) = A_{nlj \rightarrow n'l'j'} \frac{1}{e^{h\nu_{nlj \rightarrow n'l'j'}/k_B T} - 1} \quad (1.6)$$

Here the relation between Einstein coefficients  $A_{12} = B_{12} \frac{8\pi h\nu_{12}^3}{c^3}$  has been used.

In these kind of processes we are not limited to lower energetic levels, in fact thermal photons can be absorbed as well as cause stimulated emissions, therefore  $n'$  can take all the possible values. Those blackbody induced transition rates must be added to the spontaneous decay

rates to take into account all the possible channels of loss for a Rydberg atom, resulting in a lifetime expression:

$$\tau_n(T) = \left( \sum_{E_{n'l'} < E_{nl}} A_{nlj \rightarrow n'l'j'} + \sum_{n',l',j'} \frac{A_{nlj \rightarrow n'l'j'}}{e^{h\nu_{nlj \rightarrow n'l'j'}/k_B T} - 1} \right)^{-1} = \left( \Gamma^{Spont} + \Gamma^{BBR} \right)^{-1} \quad (1.7)$$

Were  $\Gamma^{Spont} = (\tau_n(0K))^{-1}$  and the total BBR depopulation rate  $\Gamma^{BBR}$  is defined as the sum of all the possible BBR induced transition rates. Introducing the oscillator strength  $f_{nl \rightarrow n'l'} = \frac{2}{3} \nu_{nlj \rightarrow n'l'j'} |\langle n'l' | \hat{r} | nl \rangle|^2$ ,  $\Gamma_{BBR}$  can be written as:

$$\Gamma_{nlj}^{BBR} = \frac{2e^2}{\hbar c^3} \sum_{n',l',j'} \nu_{nlj \rightarrow n'l'j'} f_{nlj \rightarrow n'l'j'} \frac{\nu_{nlj \rightarrow n'l'j'}}{e^{h\nu_{nlj \rightarrow n'l'j'}/k_B T} - 1} \quad (1.8)$$

Contrary to (1.4) the transitions at high frequency are depressed by the exponential denominator, for this reason the greatest contribution is given by the  $n'$  close to  $n$  with energy differences scaling as:

$$\nu_{n,n+1} \propto \left( \frac{1}{(n^*)^2} - \frac{1}{(n^* + 1)^2} \right) \sim \frac{1}{n^{*3}} \quad (1.9)$$

For  $n > 60$  the neighbouring transition frequencies are on the order of tens of GHz (see Tab(3.1)), hence  $h\nu \ll k_B T$  at room temperature. With a first order expansion of the exponential in (1.8) we obtain:

$$\Gamma_{nlj}^{BBR} = \frac{2e^2}{\hbar^2 c^3} kT \sum_{n',l',j'} \nu_{nlj \rightarrow n'l'j'} f_{nlj \rightarrow n'l'j'} \quad (1.10)$$

Moreover, according to [5],  $\sum_{n',l',j'} \nu_{nlj \rightarrow n'l'j'} f_{nlj \rightarrow n'l'j'} \sim \frac{2}{3n^{*2}}$ , so the scaling law for the complete BBR rate is  $\Gamma^{BBR} \propto n^{*-2}$ .

Comparing this scaling law to that of the spontaneous emission rate  $\Gamma_{spont} = (\tau_n(0K))^{-1} \sim n^{*-3}$ , we see that, increasing the principal quantum number, the BBR depopulation becomes more and more important with respect to the spontaneous decay processes, and, for  $n > 63$  it becomes the principal contribution of loss, as shown in Tab(1.2).

$nS$	$\Gamma_{spont}[\text{kHz}]$	$\Gamma^{BBR}[\text{kHz}]$
60	4.34	3.98
70	2.67	3.30
80	1.76	2.67
90	1.22	2.20
100	0.88	1.83

Table 1.2: Comparison of the two depopulation rates for different principal quantum numbers. For states above  $n=60$  we observe that the BBR transition rate becomes higher than the spontaneous emission one. These rates are calculated with the program ARC [16]

This sensitivity to BBR intensity makes Rydberg atoms an optimal sensor for investigating possible deviations from Planck's formula, or, in general, to sense extremely small amounts of radiations.

### 1.1.1 Repopulation processes

As a final consideration on the lifetime of a Rydberg atom, it is important to take in account the effects of repopulation. If an atom, once excited to a Rydberg state, undergoes a transition to another Rydberg state, the inverse process must be possible: the atoms lost through BBR transitions can return to the initial state.

In this brief discussion we want to derive only the order of magnitude of such processes.

If an atom in the state  $nlj$  makes a transition, the probability to jump to state  $n'l'j'$  can be rapidly estimated by:

$$P_{nlj \rightarrow n'l'j'} = \Gamma_{nlj \rightarrow n'l'j'} (\Gamma_{n,l,j}^{BBR} + \Gamma_{n,l,j}^{spont})^{-1}$$

from which we can roughly estimate the order of magnitude of the repopulation multiplying the probability to transit to an  $n'l'j'$  state by the probability to return back from that state and summing over all the possible arrival states:

$$P_{repopulation} = \sum_{n'l'j'} P_{nlj \rightarrow n'l'j'} P_{n'l'j' \rightarrow nlj} \quad (1.11)$$

This quantity is only few percent ( $\sim 4\%$ ) for the entire range of principal quantum numbers investigated, therefore we expect that it does not change the exponential decay function, but it leads only to a small alteration of the measured lifetime. A more detailed analysis of the repopulation processes will be given in chapter 4.

## 1.2 The blackbody radiation in a box

A blackbody is an ideal object that can absorb all the light that reaches it. If such an object is at thermal equilibrium with the electromagnetic field it emits radiation with spectral distribution expressed by Planck's formula:

$$u_\nu(\nu, T) = \frac{8\pi\nu^2}{c^3} \frac{h\nu}{e^{h\nu/k_B T} - 1} \quad (1.12)$$

Historically this formula was the starting point of quantum mechanics, in fact for the first time to derive the (1.12) Planck used the idea that an oscillator can have only quantised energy.

If we consider a cubic box of size  $L$ , we can calculate the resonant frequencies inside that box as

$$\nu_n = \frac{c}{2L} \sqrt{n_x^2 + n_y^2 + n_z^2} \quad (1.13)$$

Now, using the fact that the typical wavelength is much smaller than the box size  $L$ , or alternatively, considering an infinite sized box, we can calculate the number of resonant modes from  $\nu$  to  $\nu + d\nu$  per unit volume as:

$$\rho_{\text{Inf}}(\nu)d\nu = \frac{8\pi\nu^2}{c^3} d\nu \quad (1.14)$$

Finally considering that the energy distribution at temperature  $T$  of a bosonic particle is  $\Theta(\nu, T) = \frac{h\nu}{e^{h\nu/k_B T} - 1}$ , and multiplying it to the density of mode at frequency  $\nu$ , we obtain the (1.12).

### 1.2.1 The Purcell effect

A strong geometrical approximation has been made to derive the spectrum of a blackbody: the "infinite sized box" approximation. Clearly no object can be considered infinite at each scale.

The same approximation is necessary to derive also spontaneous emission A coefficient, and various studies have been performed to demonstrate corrections to spontaneous emission due to geometrical effects. The spontaneous emission can be regarded as the product of the interaction between the atom and the vacuum state of the electromagnetic field. A cavity, or in general a physical environment, can modify the vacuum state of the electromagnetic field causing alteration of the emission properties of an atom [17].

Various experiments performed with Rydberg atoms have demonstrated that the spontaneous emission of an atom can be almost eliminated [18] or strongly enhanced [19] when it is placed inside a cavity .

The Purcell effect describes such an enhancement of spontaneous emission due to modification of vacuum field state. For a cavity with quality factor  $Q$  the Purcell factor  $F_P$ , i.e. the factor which describes the enhancement of spontaneous emission rates, is defined as the ratio of the density of modes inside the cavity and that of free space:

$$F_P = \frac{\rho_{\text{Cavity}}}{\rho_{\text{Inf}}} = \frac{3}{4\pi^2} \frac{c^3 Q}{\nu^3 V} \quad (1.15)$$

As spontaneous emission, also blackbody radiation depends on the density of modes of the electromagnetic field, consequently it will be modified by the presence of a cavity.

In conclusion, in most cases the Planck formula is a good description of the thermal radiation emitted by an object, but, if the object taken into account has dimensions comparable with the wavelength of the light, the infinite sized box approximation fails and equation (1.14) needs to be corrected through geometrical considerations.

As the Planck formula is linear in the density of modes, equation (1.12) has to be corrected with the Purcell factor  $\rho_{\text{Cavity}}/\rho_{\text{Inf}}$  considering also that not all the frequencies are resonant. These corrections can be performed by directly counting the resonant frequencies within a frequency width  $\Delta\nu$ . In section 5, the deviations from Planck formula will be studied and an qualitative spectrum of blackbody radiation will be derived using such geometrical considerations.

### 1.3 Interaction with DC electric fields: the Stark effect

Another interesting property of a Rydberg atom is its strong interaction with external fields, in particular with electric fields.

Consider an electric field  $\mathbf{E} = E\hat{z}$  in the experimental volume. Using dipole approximation we can write the Hamiltonian of the atoms:

$$\hat{H} = \hat{H}_0 - \hat{d}_z E \quad (1.16)$$

If the electric field is small, i.e.  $\langle d \rangle E \ll \Delta\epsilon$  where  $\Delta\epsilon$  is the typical energy difference between near levels, we can treat this potential using perturbation theory.

We can distinguish two important cases: perturbation theory on levels with defined angular momentum and on  $l$  degenerate levels.

In light of the quantum defect for Rubidium (Tab(1.1)), the  $l > 4$  states have insignificant quantum defects, as a consequence for a given  $n$  they form a single level with a large degeneracy  $DEG_{l>4} = \sum_{l=4}^{n-1} (2l+1) = n^2 - 16$ . For example, taking  $n = 80$ ,  $DEG_{l>4} = 6384$  with 76 different angular momentum states inside. We call those levels manifolds. On the contrary S, P, D and F states, having different quantum defects, are separated in energy, consequently each level has a well-defined angular momentum, so, well-defined parity.

### 1.3.1 The quadratic Stark effect

Let us consider one of the states that are not degenerate in  $l$ , for example an S state. Well-defined parity implies that the average dipole element  $\langle nS | d | nS \rangle$  is zero. This fact means that there is no energy shift linear with the electric field.

Moreover at the first perturbative order the wavefunction becomes:

$$\Psi^{(1)} = E \sum_k \frac{\langle k | \hat{d}_z | nS \rangle}{\epsilon_k - \epsilon_{nS}} |k\rangle$$

From that we can calculate the energy shift at the second order as  $\delta\epsilon^{(2)} = \langle nS | V | \Psi^{(1)} \rangle$  that leads to:

$$\delta\epsilon^{(2)} = E^2 \sum_k \frac{|\langle k | \hat{d}_z | nS \rangle|^2}{\epsilon_k - \epsilon_{nS}} \quad (1.17)$$

defining the polarisability  $\alpha$  of a state as  $\alpha = -2 \frac{\delta\epsilon^{(2)}}{E^2}$ , from (1.17) we derive:

$$\alpha_{nS} = -2 \sum_k \frac{|\langle k | \hat{d}_z | nS \rangle|^2}{\epsilon_k - \epsilon_{nS}} \quad (1.18)$$

Using the scaling laws presented in the previous sections for energy differences of neighbouring states (1.9) and introducing the scaling law for the dipole matrix elements between neighbouring states as  $\langle n' \sim n | \hat{d}_z | nS \rangle \propto n^{*2}$ , the polarisability of a Rydberg state scales as  $\alpha \propto n^{*7}$ .

$n$	$\alpha_S [\text{MHz} \frac{\text{cm}^2}{\text{mV}^2}]$
60	$0.180 \times 10^{-3}$
85	$2.143 \times 10^{-3}$
105	$9.673 \times 10^{-3}$
120	$2.435 \times 10^{-2}$

Table 1.3: Polarisability for S and P Rydberg states of  $^{87}\text{Rb}$ . These values will be relevant for our compensation technique, described in section 2.3

### 1.3.2 The linear Stark effect

The previous description of the interaction with an electric field is no longer true if we consider a manifold in which different angular momentum states are present.

Consider a basis  $\{\beta\} = n, l, j$  with  $3 < l < n$  and fixed  $n$ , the potential  $\hat{V} = \hat{d}_z E$  connects states with angular momentum that differ by  $\Delta l = \pm 1$ , resulting, in this subspace, in off diagonal terms:

$$V = \begin{pmatrix} 0 & V_{\beta\beta'} & 0 & \dots & 0 \\ V_{\beta'\beta} & 0 & V_{\beta'\beta''} & \dots & 0 \\ 0 & V_{\beta''\beta'} & 0 & \ddots & 0 \\ \vdots & \dots & \ddots & \ddots & \vdots \end{pmatrix} \quad (1.19)$$

At zero perturbative order we can diagonalise this matrix and its eigenvalues will be the first order energy shift, so linear in the electric field [20]. This potential breaks the degeneration of the manifolds and it depicts a Stark map similar to a fan, as shown in Fig.(2.6).

The quantum defect for S states is  $\delta_0 = 3.13$ , so the  $nS$  state has energy slightly smaller than the  $n-3$  manifold. Since the energy shift of the states composing the manifold is a first order correction, it grows more rapidly with electric field than the second order shift (1.17). At a certain electric field known as Inglis-Teller limit the most downshifted of those states crosses the lower S state and for electric fields greater than this value we cannot use perturbation theory to describe the eigenstates, but an exact diagonalisation of (1.16) is required.

### 1.3.3 Ionisation thresholds

Another important characteristic of Rydberg atoms is a small ionisation threshold, consequence of the small binding energy. In this section I present a classical derivation of the electric field needed to ionise a high-lying state. For the sake of simplicity I considered a one dimensional problem with the Coulomb potential which attracts the electron toward the nucleus and an electric field in the  $\hat{z}$  direction:

$$U_{el} = -\frac{e^2}{4\pi\epsilon_0|z|} + eEz \quad (1.20)$$

Such a potential has a local maximum for  $z_{max} = -\sqrt{\frac{e}{4\pi\epsilon_0 E}}$  that is:  $U_{el}^{max} = 2e\sqrt{\frac{eE}{4\pi\epsilon_0}}$ . Classically only electrons with an energy lower than this maximum potential are bound, in other words, a first approximation of the electric field that ionises an  $n$  Rydberg state is achieved with:

$$U_{el} = \epsilon_n \quad \rightarrow \quad E_{thr} = \frac{m_e^2 e^5}{16(4\pi\epsilon_0)\hbar^4} \frac{1}{n^{*4}} \quad (1.21)$$

For the states we used in our experiments those threshold electric fields are on few tens of V/cm order, easily accessible in a laboratory.

## 1.4 Rydberg-Rydberg interactions

A natural consequence of the large dipole moments and polarisability of Rydberg atoms are the strong interactions between them.

As Rydberg atoms are neutral atoms they interact principally through dipole-dipole interaction:

$$V_{A,B}(\mathbf{R}) = \frac{1}{4\pi\epsilon_0 R^3} \left( \hat{d}_A \cdot \hat{d}_B - \frac{1}{3} (\hat{d}_A \cdot \hat{R})(\hat{d}_B \cdot \hat{R}) \right) \quad (1.22)$$

where  $\mathbf{R}$  is the vector which connects the two atoms. For large distances (Van der Waals regime) this potential can be treated as a perturbation. Consider two atoms in the state  $|nS\rangle \otimes |nS\rangle$ , as in the previous section, having well-defined parity, the first order energy shift is zero; whereas for the first order correction of the wavefunctions we have:

$$\Psi_{AB}^{(1)} = \sum_{k,k'} \frac{\langle k| \otimes \langle k'| V_{A,B} |nS\rangle \otimes |nS\rangle}{\epsilon_{k,k'} - \epsilon_{nS,nS}} \quad (1.23)$$

That leads to a second order correction of the energy of:

$$\delta\epsilon^{(2)} = \sum_{k,k'} \frac{|\langle k| \otimes \langle k'| V_{A,B} |nS\rangle \otimes |nS\rangle|^2}{\epsilon_{k,k'} - \epsilon_{nS,nS}} = \frac{\hbar C_6}{R^6} \quad (1.24)$$

The Van der Waals coefficient  $C_6$  has a scaling law which can be easily calculated from the dipole matrix element between neighbouring Rydberg states ( $\sim n^{*2}$ ) and from (1.9), resulting in  $C_6 \sim n^{*11}$ . For low-lying states this kind of interaction is negligible, in fact for ground state:  $C_6^{(GND)} = 677 \text{ nHz } \mu\text{m}^6$ , which is much smaller than the Van der Waals coefficient for a 100S state:  $C_6^{(100S)} = 1.65 \times 10^6 \text{ GHz } \mu\text{m}^6$ .

This strong interaction between Rydberg states can give rise to different excitation or de-excitation dynamics that are a disturbance in a lifetime measurement.

Using a laser of width  $\delta\nu$ , resonant with the Rydberg transition, we cannot excite two Rydberg atoms at arbitrary distances. Exciting one Rydberg atom at a given position, another hypothetical excited atom at a distance  $d$  undergoes an energy shift  $\Delta\epsilon = \frac{\hbar C_6}{d^6}$ . Therefore with a resonant laser we cannot create excitations if the Van der Waals interaction at distance  $d$  is larger than the laser width [21]:

$$\frac{\hbar C_6}{d^6} < \hbar\delta\omega \rightarrow d > \left( \frac{C_6}{\delta\omega} \right)^{1/6} = r_b \quad (1.25)$$

Here  $r_b$  is known as the *blockade radius*. In Tab(1.4) some  $C_6$  values and the correspondent blockade radii are listed:

$nS$	$C_6$ [MHz $\cdot\mu\text{m}^6$ ]	$r_b$ [ $\mu\text{m}$ ]
60	135.3	5.6
70	862.7	7.62
80	4161.4	9.91
90	16501	12.5
100	56171	15.3
105	98836	16.8

Table 1.4: Values of  $C_6$  and correspondent blockade radius calculate using the ARC Phytion library (chapter 4). To calculate  $r_b$  a laser width of  $\delta\omega = 2\pi \times 0.7$  MHz is used

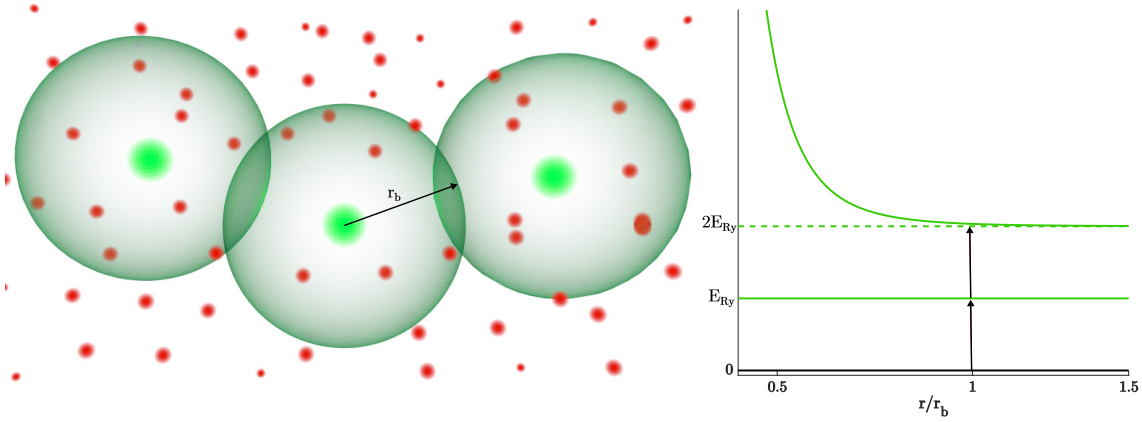


Figure 1.1: **(Left)** Schematic representation of Rydberg excitations, the red dots are atoms in the ground state whereas the larger green ones are atoms excited to a Rydberg state. The *Blockade spheres* are depicted with a transparent shade. **(Right)** Level scheme of a resonant excitation, if two atoms are less than the blockade radius apart, the interaction shifts the energy levels, hence shifting the laser out of resonance.

## 1.5 Interaction with AC Electric fields: the dressed atom approach

The *dressed atom* approach is a theoretical description of an atom interacting with intense electromagnetic radiation [22]. Approximating the atom as a two levels system we can write its Hamiltonian as:

$$H_A = -\hbar\omega_A |1\rangle \langle 1| + 0 |2\rangle \langle 2|$$

where the energy of the level  $|2\rangle$  is set to zero and we defined  $\omega_A = \frac{\epsilon_2 - \epsilon_1}{\hbar}$ . Moreover considering the electromagnetic field as a single mode field we can write  $H_L = \hbar\omega_L \hat{a}^\dagger \hat{a}$ , where  $\omega_L = \omega_A + \delta$  and  $\hat{a}, \hat{a}^\dagger$  are respectively the creation and destruction operators of a photon. The eigenstates of the uncoupled Hamiltonian  $H_0 = H_A + H_L$  are of the form:  $|1, n\rangle, |2, n\rangle$  in which the first quantum number refers to the atomic eigenstate whereas the second refers to the number of photons in the electromagnetic radiation.

The interaction potential, written using quantised electromagnetic field, is expressed in Schrödinger representation as:

$$\hat{V}_{AL} = \hat{d}\hat{E} = -i\sqrt{\frac{\hbar\omega_L}{2\epsilon_0 V}}(\hat{d}(t) \cdot e_\lambda)(\hat{a} - \hat{a}^\dagger) \quad (1.26)$$

Considering states with well-defined parity as real atomic states, the dipole operator has only off-diagonal terms and can be expressed as:  $\hat{d} = D(\sigma^+ + \sigma^-)$ , where  $\sigma^+ = (\sigma^-)^\dagger = |2\rangle\langle 1|$ . Inserting it in equation (1.26) and using the *Rotating wave approximation*, this potential couples only states  $|1, n+1\rangle$  with  $|2, n\rangle$ .

We define the single-photon Rabi frequency as  $\frac{1}{2}\hbar\Omega_0 = \langle e, 0 | \hat{V}_{AL} | g, 1 \rangle$ ; with this notation the complete Hamiltonian of the n-photons subspace becomes:

$$H = \hat{H}_A + \hat{H}_L + \hat{V}_{AL} = \hbar \begin{pmatrix} 0 & \frac{1}{2}\Omega_0\sqrt{n} \\ \frac{1}{2}\Omega_0^*\sqrt{n} & \delta \end{pmatrix} + n\hbar\omega_L \text{Id} \quad (1.27)$$

The fact that we have off-diagonal terms means that the real eigenstates of the system are no longer the bare atomic states, but a mixture of them, which are known as *dressed* states. Diagonalising (1.27) we obtain:

$$\begin{aligned} |-\rangle_n &= \frac{1}{\mathcal{N}} \left[ (\delta - \sqrt{\delta^2 + \tilde{\Omega}^2}) |1, n+1\rangle - \tilde{\Omega} |2, n\rangle \right] \\ E_- &= \hbar \frac{\delta - \sqrt{\delta^2 + \tilde{\Omega}^2}}{2} \end{aligned} \quad (1.28)$$

$$\begin{aligned} |+\rangle_n &= \frac{1}{\mathcal{N}} \left[ \tilde{\Omega} |1, n+1\rangle + (\delta + \sqrt{\delta^2 + \tilde{\Omega}^2}) |2, n\rangle \right] \\ E_+ &= \hbar \frac{\delta + \sqrt{\delta^2 + \tilde{\Omega}^2}}{2} \end{aligned} \quad (1.29)$$

Here the effective Rabi frequency is defined as  $\tilde{\Omega} = \Omega_0\sqrt{n}$  and the normalisation factor as  $\mathcal{N} = \left[ 2 \left( \tilde{\Omega}^2 + \delta^2 - \delta(\delta^2 + \tilde{\Omega}^2)^{1/2} \right) \right]^{1/2}$ .

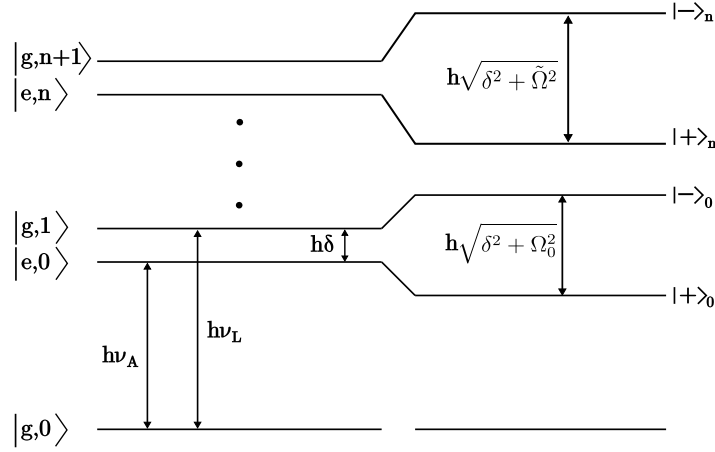


Figure 1.2: Level scheme in dressed atom approach, on the left the bare states are depicted while on the right we have the atom's levels "dressed" by the radiation.

This treatment will be useful in future analysis, in particular we can define the Autler-Townes splitting as the difference of dressed eigenenergies when the radiation is resonant with the  $1 \rightarrow 2$  transition frequency ( $\delta = 0$ ):

$$\omega_{\text{AT}} = \frac{E_+ - E_-}{\hbar} = \tilde{\Omega} \quad (1.30)$$

We exploited this splitting, as described in section 2.2.2 to perform precise Rabi frequency measurements, from which we can deduce the intensity of microwave radiation.

Furthermore, in chapter 3, I will describe the three-photon excitation, in which we couple a given S Rydberg state ( $|1\rangle$ ) with a near P state ( $|2\rangle$ ) through a detuned microwave radiation. As we will see in that chapter, an excitation of a state with a S component can lead to alteration of measurements. From (1.28, 1.29) we can define a criterium with which we can characterise the optimal Rabi frequency to use in order to neglect the presence of state  $|1\rangle$  in  $|-\rangle$  that represent the Rydberg P state in the limit  $\frac{\tilde{\Omega}}{\delta} \rightarrow 0$ .

We can define  $f$  as the probability to be projected onto  $|1\rangle$  divided by the probability to be projected onto  $|2\rangle$ , once we have excited 1 atom in the dressed state:  $f = \frac{P_1}{P_2} = \frac{|(1|-\rangle|^2}{|(2|-\rangle|^2}$ . Imposing that this ratio must be smaller than a certain  $f_{\text{MIN}}$  we obtain:

$$\frac{(\delta - \sqrt{\delta^2 + \tilde{\Omega}^2})^2}{\tilde{\Omega}^2} < f_{\text{MIN}} \quad \rightarrow \quad \tilde{\Omega} < \frac{2\delta\sqrt{f_{\text{MIN}}}}{1 - f_{\text{MIN}}} \quad (1.31)$$

As an example, posing  $f_{\text{MIN}} = 10^{-2}$ , we can use coupling Rabi frequencies up to  $\tilde{\Omega} < \frac{\delta}{5}$

## Chapter 2

# Description of the experimental set-up

After the theoretical introduction of the physical processes investigated during my thesis work, in this chapter I will describe the experimental set-up used to study them experimentally. Starting with a brief description of the cooling and trapping system I will proceed to clarify the set-up and the techniques for the Rydberg excitation, the state-selective de-excitation and the electric field compensation that allowed us to measure the lifetime of different angular momenta, high-lying Rydberg states. In the end of this chapter I will explain the stabilisation of our Fabry-Pérot interferometer from external perturbations achieved with a stepper motor.

### 2.1 Trapping and detecting systems

#### 2.1.1 The Magneto optical trap

In the field of quantum gases, *laser cooling* is nowadays a standard technique to reduce the width of the momentum distribution of neutral atoms and consequently to reach very low temperature of gaseous samples. Using well-designed, inhomogeneous electromagnetic fields it is possible to confine atoms in a small region of space, so combining these two techniques we can create high-densities clouds of cold atoms.

With the aim of measuring the lifetime of various Rydberg states, we do not need a system with extreme properties such as temperatures of the nanokelvin order or densities of  $10^{17} \div 10^{18} \frac{\text{atoms}}{\text{cm}^3}$ , which are parameters easily accessible in a cold atom laboratory exploiting Bose-Einstein condensation. The lifetime of the investigated Rydberg states is expected to vary in the range from about 100 to 400 microseconds [23], so, to correctly measure these

quantities, a stability on the order of few milliseconds is needed. Moreover, high densities are not required because short distances between atoms could cause undesired interaction processes.

These conditions are realised with a standard cooling and trapping scheme known as Magneto-Optical Trap (MOT), for which a detailed theoretical description can be found in the literature [24], and precise characterisation of our apparatus can be found in [25].

Three pairs of counter-propagating lasers along mutually perpendicular directions are used to cool down the gas exploiting absorption-spontaneous emission cycles. The laser frequencies must be red detuned from the selected transition frequency in order to exploit the Doppler effect: an atom with a velocity  $\mathbf{v}$  sees the incoming photons frequency shifted. More precisely it sees the photons red shifted if they are travelling in  $\hat{v}$  direction and blue shifted if they are travelling in  $-\hat{v}$  direction, resulting in greater absorption probability for the second kind of photons. Each absorption of those photons adds to the atoms momentum a term  $\hbar\mathbf{k}\cdot\hat{v} = -\hbar k$  whereas a spontaneously emitted photon subtracts the same term but in a random direction. If this process is repeated for a significant number of times, no momentum recoil is acquired from the spontaneously emitted photons on average, resulting in a net momentum transferred to the atoms, which decreases atoms velocity. In a semiclassical treatment, these recoil processes are schematised with a friction force that decreases the width of the atomic momentum distribution and consequently the temperature of the cloud down to the *Doppler limit* [26]. Furthermore, the cooling procedure is also made space dependent by exploiting the Zeeman effect. We use a pair of coils with currents flowing in opposite directions (*Anti-Helmholtz* configuration) which generate a quadrupole magnetic field. Near the center of this scheme the magnetic field can be approximated as  $\mathbf{B}(x, y, z) = b'(x, y, -2z)$  where we use  $b' = 12.2$  G/cm. In the same semiclassical treatment, the space-dependent recoil processes cause an harmonic force that is added to the viscous one confining the atoms around the center of the quadrupole.

Our experiments are performed with  $^{87}\text{Rb}$  atoms, in an ultra-high-vacuum cell where a pressure of about  $10^{-10}$  mBar is maintained. The main trapping laser has a wavelength of 780 nm to couple the  $|5S_{1/2}, F = 2\rangle$  ground state to  $|5P_{3/2}, F = 3\rangle$  state. This beam is produced by a diode laser and locked to the atomic transition using a saturated absorption scheme [27]. Another *repump* laser is produced and frequency stabilised with a similar scheme and locked to the  $|5S_{1/2}, F = 1\rangle \rightarrow |5P_{3/2}; F = 2\rangle$  transition frequency. This beam is necessary in order to pump atoms decayed in the  $F = 1$  ground state, that is a dark state for the trapping laser, back into the  $F=2$  ground state. A MOT scheme and the involved transitions are depicted in Fig.(2.1).

Using this apparatus we are able to produce cold Rubidium clouds of gaussian shapes with

typical dimensions :  $\sigma_y \sim \sigma_x = 300 \mu\text{m}$ ,  $\sigma_z = 180 \mu\text{m}$ , typical numbers of atoms of about  $N = 10^5 \div 10^6$ , so densities around  $\rho = \frac{N}{(2\pi)^3 \sigma_x \sigma_y \sigma_z} = 10^{10} \div 10^{11} \text{ atoms/cm}^3$  and finally temperatures of  $T = 100 \div 150 \mu\text{K}$ . To measure these quantities, we have a high-resolution CCD camera pointed toward the MOT that measures the intensity spontaneously radiated by the atoms in the trapping cycles and a LabView program computes the number of atoms, the MOT dimensions, and its position.

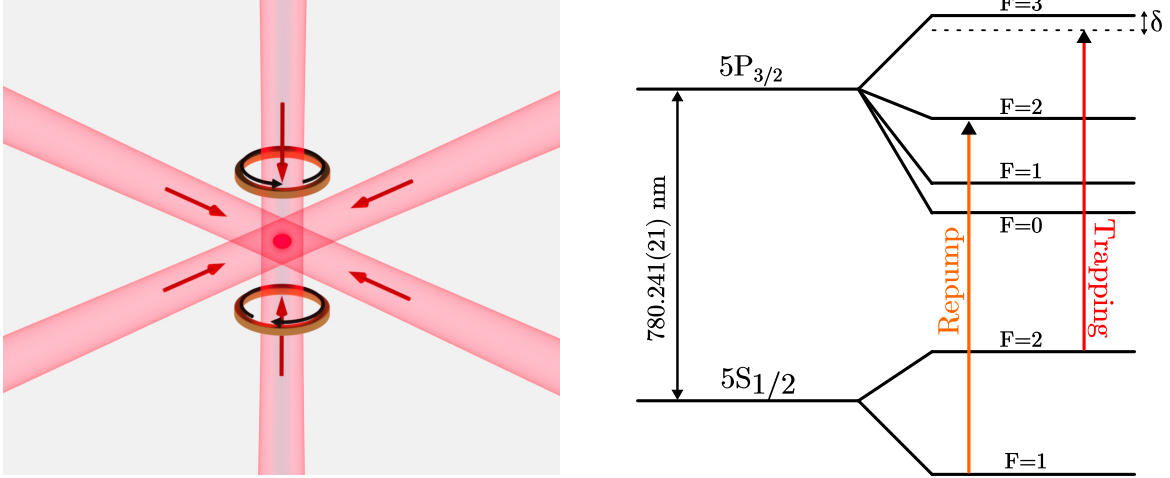


Figure 2.1: **(on the top)** Simple scheme of the Magneto Optical Trap, where the three counter propagating lasers and the coils in Anti-Helmoltz configuration are depicted. **(on the bottom)** The hyperfine structure of Rubidium 87 and the transition frequencies used in the trapping and repumping processes. The detuning of the trapping laser is  $\delta = -2.9\Gamma_{5P_{3/2}}$  where  $\Gamma_{5P_{3/2}} = 2\pi \times 6.0666(18) \text{ MHz}$  is the linewidth of the  $|5P_{3/2}\rangle$

### 2.1.2 Detection system

After this brief explanation of the preparation of the cold atomic sample, we turn to the description of the detection system.

Six pairs of electrodes, realised with foils of brass, are placed just outside the quartz cell in which the MOT is created, as is depicted in Fig.(2.2)

To detect Rydberg atoms we use a destructive ionisation measurement. We apply a  $9 \mu\text{s}$  high voltage pulse of 3, 5 kV on the *frontal plates* and  $-1 \text{ kV}$  on the *lateral plates*. These HV pulses generate an electric field, at the MOT position, greater than the ionisation threshold for states with principal quantum number above 60. After being ionised, the free ions are accelerated towards the end of the cell (red line in Fig(2.2)).

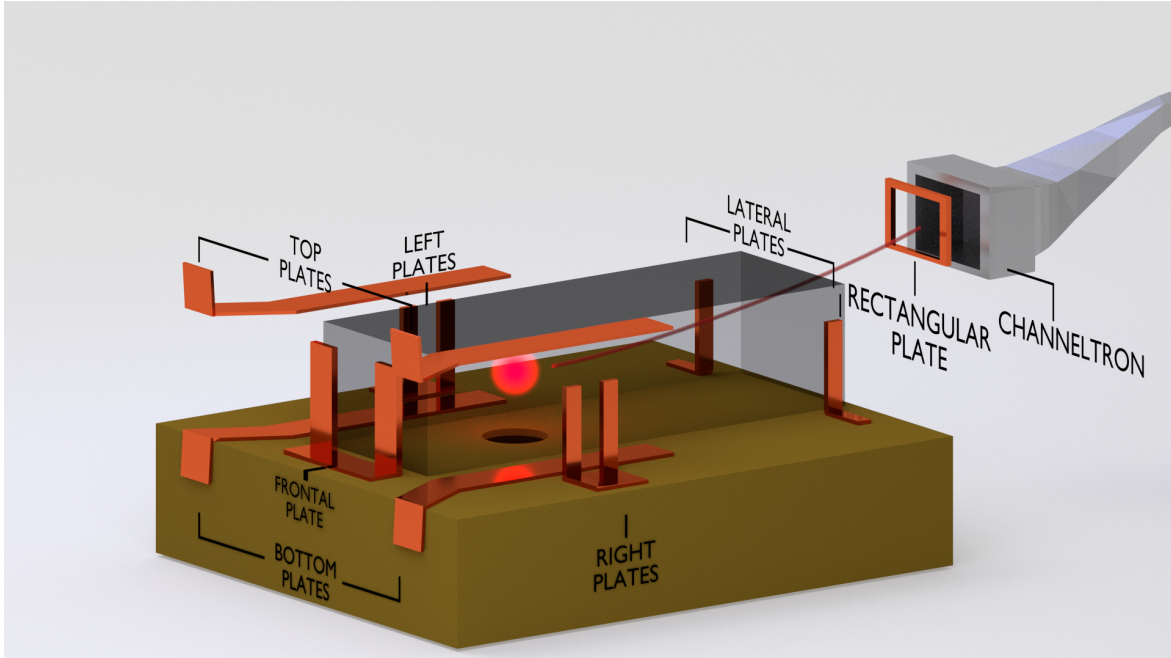


Figure 2.2: Scheme of the plates disposition around the vacuum cell. The Frontal and Lateral plates and the Rectangular electrode are used to field ionise the Rydberg states and adjust its trajectory represented with a red line starting from the MOT. The Channeltron and the rectangular electrode are located inside the vacuum system that is not completely represented in this scheme. The other plates will be useful for the electric field compensation which will be described in section 3.3. The image was realized using a 3D modelling software called Blender.

Another high voltage pulse is applied on the rectangular electrode, that deviates the ions trajectory and directs them toward a channel electron multiplier (Channeltron) *Dr Sjuts Optotechnik GmbH-KBL510*.

When an electron hits the internal surface of the Channeltron, several electrons are emitted for secondary emission processes. The new electrons are accelerated again by an internal bias field and hit again the active surface. In this way an avalanche process is triggered and at the end of the Channeltron a measurable electric signal is generated. This signal is sent to an oscilloscope *LeCroy WaveRunner-104M Xi* and analysed by means of a LabView software.

With this ionisation scheme we are able to directly count the number of excited Rydberg atoms in states above  $n=60$ , with an efficiency of about 40%. We have checked that above that threshold the detection efficiency is largely independent of  $n$ .

The calibration of the Channeltron and the ionisation voltages are described in [28].

## 2.2 Excitation techniques

Rubidium Rydberg states could be excited using a single UV photon, but, this kind of process allows only P state excitations. In order to achieve different angular momentum states we decided to perform multiphoton excitations. As I will explain in detail in this section, the S and D states are excited through two-photon processes, whereas, the P states are excited through three-photon processes.

### 2.2.1 Excitation laser set-up

Once the atoms are trapped, we are able to drive a two-photon transition from ground state ( $|5S_{1/2}; F = 2\rangle$ ) to  $|n_{Ry}S_{1/2}\rangle$  state with  $|6P_{3/2}; F = 3\rangle$  as intermediate energy level, using a blue laser and an infrared laser with wavelengths respectively of about  $\lambda_{Blue} = 420$  nm and  $\lambda_{IR} = 1012$  nm.

The first laser is an assembled system *Toptica-TASHG pro* which consists of an 840 nm diode laser *DL-100* that is amplified by a tapered amplifier *TA-100* and frequency doubled through a *SHG-1004* non-centrosymmetric crystal exploiting second harmonic generation. The second laser is a *Toptica-DL110*, that consists only in a single diode laser which is amplified through a tapered amplifier *Sacher Lasertechnik-TIGER*.

Both lasers have an external cavity made by a diffraction grid that injects the  $-1$  order in the active medium and the zeroth order is used as output beam (*Littrow scheme*). The orientation of this external cavity is regulated by a piezoelectric crystal, so we can tune the resonant frequency acting on this device.

In order to monitor the frequency of both lasers, small parts of the 1012nm and the 840nm lasers are injected in a Fabry-Pérot (FP) interferometer together with part of the trapping laser. The 780 nm laser is stabilised on an atomic resonance, and used as a reference for the excitation lasers.

A software programmed in *LabView* reads in loop the output signal of the FP measuring the distance of the two excitation lasers from the 780nm laser in units of *Free Spectral Range* (FSR) of the cavity, that is 1 GHz. Moreover, this program allows us to lock blue and IR frequencies to a given distance from the reference or change it with a resolution of 0.5 MHz by sending a feedback signal to the piezo on their external cavities.

This system doesn't give us any information about the absolute wavelengths of the excitation lasers which are measured through a wave meter with resolution of  $\sim 1$  pm.

The lasers are sent to the cloud co-propagating in the  $\hat{x}$  direction and have gaussian profile with waists respectively :  $w_{Blue} \sim 40 \mu\text{m}$  and  $w_{IR} \sim 90 \mu\text{m}$ . The excitation volume is defined in the x direction by the MOT dimension  $\sigma_x$  and, in the perpendicular directions, is defined

by the overlapping of the excitation lasers and the spatial profile of the MOT as follows:

$$V_{exc} = \int_{-\infty}^{\infty} e^{-\frac{x^2}{2\sigma_x^2} - \frac{y^2+z^2}{2w_{Blue}^2}} d^3x = (2\pi)^{3/2} w_{Blue}^2 \sigma_x = 7.56 \times 10^6 \mu\text{m}^3 \quad (2.1)$$

The procedure to find the resonant frequency for exciting an S Rydberg state involves two steps:

- Blue frequency scan

In the first stage we tune the blue laser to the intermediate  $|6P_{3/2}, F = 2\rangle$  state. Using the HV pulses presented in the previous section, states with  $n$  lower than 60 cannot be ionised therefore our detection system, based on ions counting, cannot reveal them. For tuning this laser, we use a second order transition: the absorption of two 420 nm photons directly photo-ionises a Rubidium atom and the ion is detectable. The more the frequency is tuned to  $|5S_{1/2}; F = 2\rangle \rightarrow |6P_{3/2}; F = 3\rangle$  transition, the more efficient the process.

We perform this measurement using a blue power of about  $P_{blue} = 0.3$  mW and setting the high voltage pulses immediately after the excitation. By means of the FP Lab View program we operate a fine tuning of the laser frequency locking it at a precise distance from the reference.

- IR frequency scan

Once the first resonance frequency is found, we turn to the Rydberg resonance search, tuning the IR laser frequency. We excite Rydberg states with a direct two-photon excitation, in which the 420nm laser is blue detuned by  $\delta_{Blue} = 37$  MHz. Acting on a screw on the external cavity of the IR laser we coarsely change its wavelength which is monitored by means of the wave-meter. We set it as close as possible to the desired theoretical value and, after that, a more precise tuning is realised adjusting the temperature and the current of the laser diode. We used wavelengths from  $\lambda_{120S} = 1011.108$  nm to  $\lambda_{60S} = 1013.763$  nm.

Finally, we operate a fine tuning by using again the FP program as above, with the resonant condition being:

$$\nu_{IR} + \delta_{Blue} = \frac{\epsilon_{nRy} - \epsilon_{6P_{3/2}}}{h} \quad (2.2)$$

For this measurement, we typically use a blue power of  $P_{Blue} = 30$   $\mu$ W and an infrared power of  $P_{IR} = 0.8$  mW.

Using second order perturbation theory it is straightforward to calculate the Rabi frequency

for this process as:

$$\Omega_{2-photon} = \sqrt{\frac{\Omega_{Blue}^2 \Omega_{IR}^2}{(2\pi\delta_{Blue})^2} + (2\pi\delta_{IR})^2} \quad (2.3)$$

Here I defined  $\Omega_{Blue} = \frac{1}{2} \frac{E_{Blue} d_{5S-6P}}{\hbar}$ , similarly  $\Omega_{IR} = \frac{1}{2} \frac{E_{IR} d_{6P-nRy}}{\hbar}$ , and finally the overall detuning  $\delta_{IR} = \nu_{IR} + \delta_{Blue} - \frac{\epsilon_{nRy} - \epsilon_{6P_{3/2}}}{h}$ .

Once atoms are excited to the target Rydberg state we have the possibility to selectively de-excite that state performing a laser pulse resonant with  $|6P_{3/2}; F=2\rangle$  state which has a lifetime of about 120 ns, so every atom driven in this state rapidly decays to the ground state. A more detailed description of the de-excitation technique will be given in section 3.2. In order to shift the IR frequency, we use a *Cat-eye* [29] scheme: the laser, which has linear polarisation, passes, in sequence, through a Polarising Beam-Splitter (PBS), an Acousto-Optic Modulator (AOM), a lens, a  $\lambda/4$  plate and finally hits a back reflecting mirror as depicted in Fig.(2.3). The AOM is a device that couples acoustic modes of a medium, driven by an external sinusoidal signal at  $\nu_{RF}$ , and light modes. Exploiting the acousto-optic effect it creates a diffraction pattern in which the  $n$ th order is frequency shifted by  $n\nu_{RF}$ , with intensity in each order depending on the phase matching chosen and on the number of phonons present, controlled by the intensity of the radiofrequency sent.

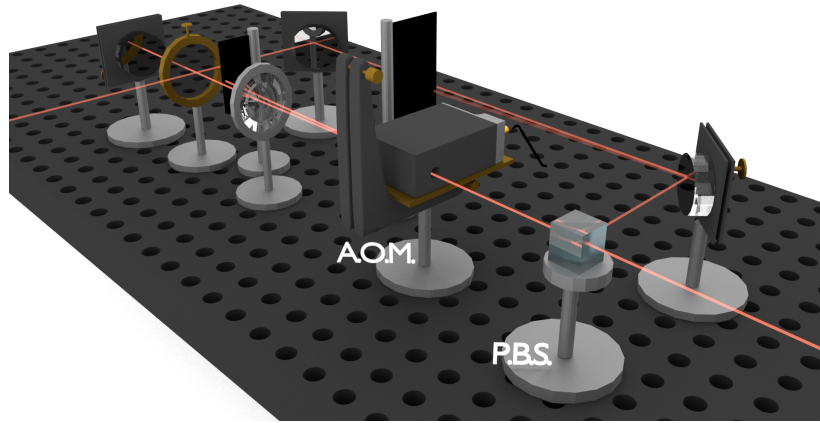


Figure 2.3: Schematic representation of the optics disposition in the Cat-eye scheme. Only the zeroth and first order of diffraction for both the first and second passages are depicted. As described the zeroth order is the beam that is blocked by the dark sheets of paper. The image was realized using a 3D modelling software called Blender.

The diffraction angle is linear with the frequency of the driving signal, and for  $\nu_{RF} \sim 70$  MHz it is several milliradians. The phase matching in this scheme is chosen to have the

maximum power achievable on the +1 order, furthermore, the other orders are stopped by a black sheet of paper.

The beam is reflected back by the mirror towards the AOM and it is aligned to superpose with the incoming beam, maximising again the +1 diffraction order. If this alignment is perfectly realised, changing the driving radiofrequency causes no alteration of the optical path after the second passage through the AOM. Now the beam, being passed two times across the  $\lambda/4$  plate, has polarisation rotated by 90 degrees and is reflected by the PBS.

This scheme is useful for three reasons: first if no radiofrequency is sent to the AOM the beam is blocked and no light reaches the experimental volume. This fact makes the Cat-eye an optimal switch for the laser and allows us to define precise excitation times.

Moreover, the laser frequency could be rapidly shifted by  $+2\nu_{RF}$  acting on the radiofrequency signal without altering the optical path followed.

Finally this scheme acts also as a power controller for the laser light, because acting on the amplitude of the sinusoidal signal we can control the diffraction efficiency and consequently the intensity of the light that arrives at the atoms.

### 2.2.2 Microwaves set-up

The techniques explained above enable us to excite and de-excite atoms to S or D Rydberg states. In order to excite P Rydberg states, we cannot use two-photon transitions because we start from an S ground state and electric dipole selection rules prevent us from reaching a P state; on the other hand, a single photon transition cannot be achieved with our lasers. We explored two different excitation schemes, both including a third microwave photon:

- $\pi$  pulses from a near S state
- Direct three-photon excitation

The former method is more complicated than the latter: starting from a population in the S state, a perfect  $\pi$  pulse is required if we want to ensure a pure P state population. With our apparatus this condition turns out to be unfeasible and an S cleaning depump pulse is necessary. By contrast if we use a direct three-photon excitation we are able to create only P excitations and for this reason in the following discussion I will treat only the second procedure.

Working with states with  $n$  in the range from 60 to 100 we can exploit transitions to neighbouring P states with frequencies from 1 GHz to 15 GHz. We use a microwave signal generator *DL Instrument-SG6800HF* to generate signals of such frequencies with widths of about 500 Hz. The continuous-wave output of the synthesiser is formed into pulses using a microwave

switch *UMCC SR-S400-1S-A2* driven by a TTL pulse. Then this signal is sent to the atoms using a helix antenna for frequencies below 10 GHz and a cylindrical antenna for frequencies above 10 GHz, both placed at about 50 cm from the vacuum cell.

Using different frequencies, it is difficult to know exactly what radiative power arrives at the atoms due to the fact that different wavelengths imply different emission properties of the antennas. Although we have no direct way of measuring microwave powers, we can determine the microwave intensity at the position of the MOT by observing the Autler-Townes splitting (1.30) when the microwaves are tuned to a selected transition [30].

In order to excite a P Rydberg state we perform, at first, a blue and an infrared frequency scan in which we drive the AOM in the cat-eye with  $\nu_{RF} = 43$  MHz. After that, we switch the radiofrequency to  $\nu_{RF} = 57$  MHz posing  $\delta_{IR} = 28$  MHz and we raise the IR power to about  $P_{IR} \sim 11$  mW. In spite of the higher power, we don't create excitations in the S state because of the large detuning.

With those new parameters, we perform a *microwave frequency scan*, finding the resonant frequency that fulfils the condition:

$$\nu_{MW} + \delta_{IR} = \frac{\epsilon_{n'RyP} - \epsilon_{nRyS}}{h} \quad (2.4)$$

The Rabi frequency for this process is calculated, using third order perturbation theory (Appendix A1), as:

$$\Omega_{3-photon} = \sqrt{\frac{\Omega_{Blue}^2 \Omega_{IR}^2 \Omega_{MW}^2}{(2\pi\delta_{Blue})^2 (2\pi\delta_{IR})^2} + (2\pi\delta_{MW})^2} \quad (2.5)$$

Where as above I defined  $\Omega_{MW} = \frac{1}{2} \frac{E_{MW} d_{n'RyP-nRyS}}{h}$  and the new overall detuning  $\delta_{MW} = \nu_{MW} + \delta_{IR} - \frac{\epsilon_{n'RyP} - \epsilon_{nRyS}}{h}$ . I worked only with transitions involving  $n' = n$  or  $n' = n \pm 1$ .

Particular attention must be paid to the value of  $\Omega_{MW}$  because, if it is comparable with  $\delta_{IR}$ , the microwave radiation "dresses" the atom and the new eigenstates become those described in section 1.5. Those new eigenstates are a mixture of the  $|nRyS\rangle$  and the  $|n'RyP\rangle$  states. After the excitation time, when the microwaves are turned off, the dressed states are projected onto the bare states and a net population in the S state could be created. In order to avoid this mixing we typically use  $\Omega_{MW}$  of about  $2\pi \times 1 \div 2\pi \times 5$  MHz. Using equation (1.31) we can evaluate the presence of  $|nRyS\rangle$  state in the dressed state that results lower than  $f < 1\%$ .

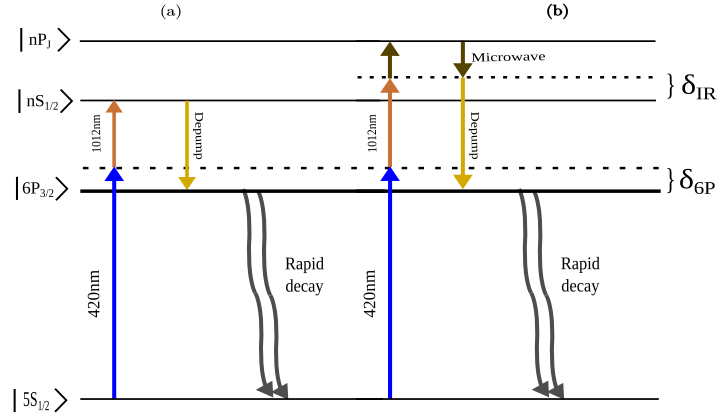


Figure 2.4: **(a)** Level scheme for the excitation (on the left) and de-excitation (on the right) of an S Rydberg state. **(b)** Level scheme for the excitation (on the left) and de-excitation (on the right) of a P Rydberg state. As already discussed the blue laser is detuned by  $\delta_{Blue} = 37$  MHz during the excitation of a Rydberg state whereas the infrared laser is resonant in (a) and is detuned by  $\delta_{IR} = 28$  MHz in (b).

The coupling with microwaves, if strong, causes an AC Stark shift (1.28). We can evaluate immediately by means of the microwave frequency scan if the microwave power is too high, observing the difference of the experimental resonant frequency from its theoretical value. This quantity is also affected by a DC Stark shift, as I will expose in the next section. The presence of stray electric field is also monitored by this measurement. If a significant deviation from the theoretical value is measured although a low microwave power, we understand that an electric field compensation is needed.

In Fig.(2.5) the differences from theoretical values that we observed in our experiments are shown. Since all the reported values are compatible with zero we can argue that no significant energy shifts were present during the experiments.

In order to monitor the presence of population in the S state we use the following procedure: in a first measurement we set the frequencies as in (2.4) and we measure the number of excited atoms. In a second measurement, after the exciting process we operate a de-excitation pulse of only infrared light tuned to the transition frequency  $|nRyS\rangle \rightarrow |6P_{3/2}, F=3\rangle$  as I will expose in detail in section 3.2. If we have atoms in the S state, this pulse drives almost all of them to the intermediate 6P state from which they rapidly decay to ground state. After that we count again the remaining population. If no significant population difference is observed between the two measurements, we have a pure P state sample. I report two depump measurements in Fig.(2.5), one in presence of high microwave power in which a net population is created in the S state, and the other that is the same measurement but with lower microwave power in which the population is only in the P state.

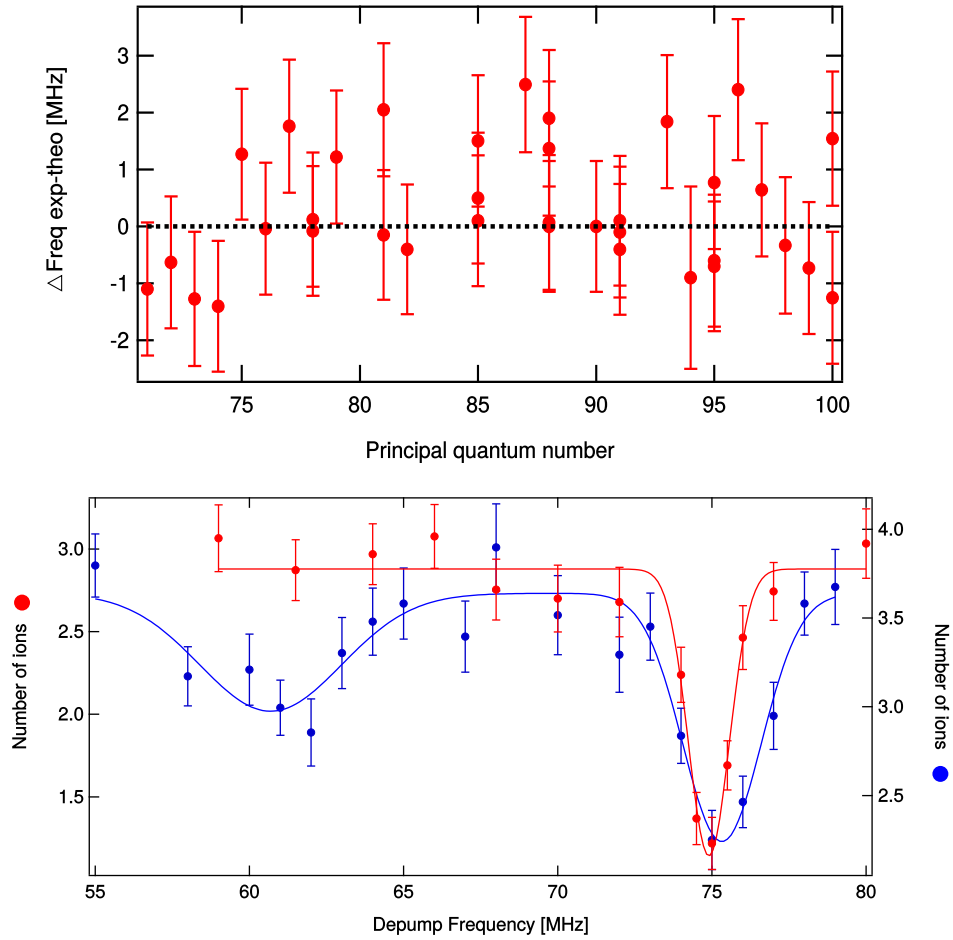


Figure 2.5: The **upper graph** refers to the difference of the measured transition frequency from  $nS$  to  $nP$  states, with respect to theoretical values calculated with ARC (explained in section 4.1). The bottom axis refers to the principal quantum number of the excited  $P$  state. The error is evaluated considering the resolution on the frequency of the IR laser and the RF signal. The **lower graph** shows two depump frequency scan in which we de-excite the target  $P$  state as explained in the next chapter. At 75 Mhz we theoretically de-excite the target  $P$  state whereas at 61.5 MHz we de-excite the intermediate  $S$  state. From (1.31) we derive that the microwaves Rabi frequency for the measurement reported in blue is  $\sim 24$  MHz whereas for the red dots we do not see any depression around 61.5 MHz, sign of a correct  $P$  state excitation.

### 2.3 Stray electric field compensation

Rydberg atoms, as already mentioned, have extreme properties. This fact is very interesting for various purposes but sometimes it can lead to problems during the experiments. An example is the high polarisability combined with the very small energy distance between different levels. If very small, uncontrolled electric fields are present in the experimental volume a Rydberg state can strongly couple with it. As defined in section 1.3.2, if the absolute value of the electric field is greater than the Inglis-Teller limit for the target state, perturbation theory is no longer valid. Diagonalising the Hamiltonian in the presence of an electric field Fig(2.6(b)), we see that, as soon as the energy of the target crosses the lower manifold state energy, the state we want to excite has several component with high angular momentum. In such a situation both the measured target and the ensemble lifetime are completely different from the expected values [9].

In order to measure the absolute value of the stray electric field, we perform a Stark map measurement of the state 85S. We raise the lasers power to  $P_{Blue} = 0.3$  mW and  $P_{IR} = 60$  mW in order to excite all the states that are slightly mixed with the 85S. Then we measure the distance from the target state to the lowest energy state of the 82 manifold Fig.(2.6(a)). This distance is compared to the theoretical Stark map calculated using ARC, a Python package that will be explained in chapter 4. We estimated, in our apparatus, a stray electric field at the MOT position of about 215 mV/cm. Although it appears small compared to the ionisation one, it is enough to oblige us to work below principal quantum number  $n=77$ .

In order to reduce this stray field as much as possible, we use the six electrodes shown in Fig.(2.2). We apply voltage pulses separately on the Frontal, Right and Inferior plates and the other three pairs are maintained to ground voltage. The disposition of the plates is chosen in such a way that we can approximately generate electric fields in every direction.

The voltage pulses must be short enough in order not to polarise the quartz cell but long enough to cover all the experimental dynamics: in fact, we turn on the compensation fields 200  $\mu$ s before the Rydberg excitation and we turn them off 1.7 ms after. To generate those voltage pulses we use 3 different generators, each one linked to an opto-coupler, driven by the same TTL pulse.

The stray electric field is not stable for a long time, in fact, we check it weekly. Keeping fixed the minimum voltages of the last compensation, we examine the state 105S which has a polarisability of  $\alpha_{105S} = 9.673 \times 10^{-3} \text{ MHz} \frac{\text{cm}^2}{\text{mV}^2}$ . This high polarisability implies that if we change the electric field by 10 mV/cm that state undergoes a Stark shift of about  $\sim 0.5$  MHz that is measurable with our set-up.

Once we have found the resonance we change one plate voltage keeping fixed the other two

and we measure the resulting Stark shift. With this protocol, we can trace the Stark parabola:

$$\delta\epsilon = -\frac{1}{2}\alpha_{105S}\left((E_i - E^{\text{applied}})^2 + E_{\perp}^2\right) \quad (2.6)$$

Here  $E_i$  is the electric field in the direction we would compensate,  $E^{\text{applied}}$  is the electric field generated by the pair of plates and  $E_{\perp}$  is the electric field in the other directions. Considering that for an S state  $\alpha$  is positive, choosing the voltage that maximises its energy we expect that  $E^{\text{applied}} = E_i$ , so the electric field in the selected direction is around zero. Repeating this process for each pair of plates we compensate as far as possible the stray electric field.

In order to measure the residual electric field, after compensating the three directions, we can use the same protocol applied to measure the absolute value of the stray electric field. Using 85S state we do not see any coupling with the manifold levels. For this reason we chose a 120S state which has the Inglis-Teller limit around  $E_{120S}^{I-T} \sim 18$  mV/cm.

From the results exposed in Fig(2.6(c)) we see the first 117-manifold peak is at higher energy than 120S state, consequently we can infer an electric field lower than  $E_{120S}^{IT}$ , estimated to be  $17 \pm 5$  mV/cm.

To understand how small that field is, we can estimate the number of electrons  $N$  which lying on the external surface of the vacuum cell could cause such an electric field. The external dimensions of the vacuum cell is  $2.4 \times 3 \times 9$  cm, considering for example  $d = 3$  cm, we found:

$$17 \frac{\text{mV}}{\text{cm}} = \frac{k_0 N e}{d^2} \rightarrow N \sim 10^6 \quad (2.7)$$

Deputatova *et al.* [31] have found that this is the order of magnitude of the free charges on a single particle of dust.

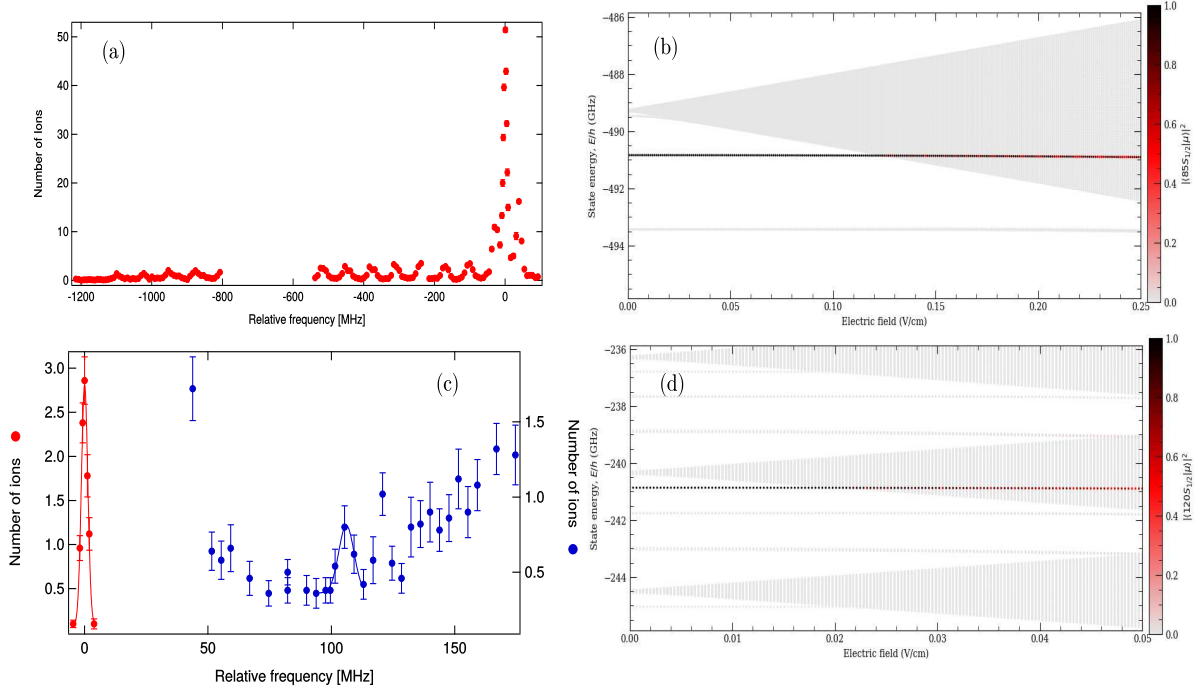


Figure 2.6: **(a)** Stark map measurement of the state 85S without compensation fields: the lowest manifold state is found at  $\sim 1.1$  GHz. **(b)** Theoretical Stark map for 85S as a function of the electric field. The energy distance of 1.1 GHz mentioned above corresponds to  $215 \pm 5$  mV/cm **(c)** Stark map measurement of the state 120S with compensation fields applied. The red curve is the direct excitation of the 120S and is taken with lower lasers power than the blue one. The lowest manifold peak is found above the 120S resonance of about 100 MHz. At higher frequencies we cannot resolve different states but the higher measured number of ions with respect to the region from 60 MHz to 100 MHz highlights the excitation of manifold levels. **(d)** Stark map of the 120S as a function of the electric field, the conditions in (c) correspond to a residual electric field of  $17 \pm 5$  mV/cm.

## 2.4 Fabry-Pérot stabilisation

Our Fabry Pérot interferometer is a *Toptica- FP100* and essentially it is a confocal cavity where a piezoelectric is displaced behind one of the two mirror in order to move it and consequently change the resonant frequency of the cavity. The piezo is driven by a triangular wave and the output signal is acquired in a sweep of that wave.

During the experiment we see slow variations in time of the reference position; being stabilised on an atomic resonance we certainly know that the trapping laser frequency changes are smaller than the observed shifts. We attribute this position variation to instabilities of

the piezoelectric crystal. Theoretically, if the crystal were working in linear regime, at the beginning of the slope the mirror should always be in the same position, and the acquired signals, excluding lasers frequency changes, should be the same.

The instability of this apparatus could be due to a different response of the piezo that is sensitive to external perturbations like humidity changes, temperature changes or external vibrations, or alternatively hysteresis effects could lead to changes in the centre of oscillation for the piezoelectric elongation.

In our system, the FP stability is crucial to ensure the stability of the excitation lasers frequencies. These lasers are locked by means of the LabView software to a precise distance from the reference, with any change in the latter position causing a small frequency shift of the excitation lasers.

In order to automatically correct a shift of the reference position, I realised a mechanical feedback on the handle controlling the offset of the triangular wave. I used a stepper motor that is a permanent magnet enclosed by 8 different coils. When a current pulse passes through the coils it generates a magnetic field that changes the orientation of the magnet. Moreover I exploit a driver circuit to generate signals in such a way that a single pulse changes the orientation of the magnet by about  $\frac{1}{16}^\circ$ . In order to operate the driver 3 signals are needed: the  $\overline{ENABLE}$  (EN), the DIRECTION (DIR), and the STEP. I fixed the stepper motor to the offset handle in such a way that a rotation of the magnet involves a rotation of the handle. The LabView program, in a loop cycle, operates in the following way: it acquires the signal from the FP, it fits the curve and records the centre of all the lasers peaks. After that, it calculates the distance between the two order of the reference, defining the free spectral range, and it calculates the distances from the first order of the reference to the other two lasers.

I generate an acceptability range for the second order of the trapping laser, and in an additional step of the loop cycle it checks if the position of that peak is acceptable. If this condition is not fulfilled, a LabView VI called Motor-Control is triggered and the three needed signals are generated. When the step pulse arrives at the stepper, it turns the magnet in the desired direction and consequently the offset handle that compensates the position shift. Using this system I improved the stability of our apparatus from few tens of minutes to entire day.

## Chapter 3

# Measurement of the S, P and D Rydberg state lifetime

Measuring the lifetime of Rydberg states is challenging. At first we must be sure to avoid the excitation of a mixed state, monitoring experimental conditions such as the presence of external fields or interaction processes. Furthermore, although we excite a population in a single state, during the evolution various states, very close in energy, are populated via BBR induced transitions. Therefore a state-selective detection technique is required to distinguish the state we want to measure from the others.

In this chapter I will outline the experimental conditions used to achieve the single state regime, then, I will discuss the de-excitation of S, P and D Rydberg states, the technique used to selectively detect our target state. After that I will describe the technique used to perform lifetime measurements of S and D states showing the experimental results obtained. This procedure was the central argument of the thesis work of A.Greco and a more detailed description can be found in his thesis [11].

Finally I will show the lifetime measurement procedure for P states discussing the experimental results in light of the previous exposed data.

### 3.1 Experimental conditions

As shown in chapter 1 the extreme response of high-lying states to electric fields can lead to strong mixing between target state and manifold levels. For this reason before the beginning of each experiment, we must ensure that the electric field present in the vacuum cell is well-compensated, otherwise, the measured lifetime is considerably different from theoretical predictions [9].

If the electric field is maintained smaller than the Inglis-Teller limit for the investigated state, no mixing with manifold states is produced and only a first order correction of wavefunctions is caused. As demonstrated in chapter 2 we are able to reduce the electric field up to  $E_{\text{Res}} \sim 17 \text{ mV/cm}$ , which allows us to work with principal quantum numbers up to 120. Furthermore, we have to be sure that at the beginning of the excitation process all the atoms are in the ground state 5S. The absorption of a 420nm photon from the 5P state directly photo-ionises the atom and, considering our detection technique based on ionised atoms counting, those free ions alter our results. In order to prevent false counts, we perform our experiments without the presence of trapping lasers switching them off 2 microseconds before excitation.

After the trapping lasers are switched off, the atomic cloud expands with a mean velocity which is, at  $T = 100 \text{ } \mu\text{K}$ ,  $\langle v \rangle = \sqrt{\frac{3k_B T}{2m_{Rb}}} \sim 120 \text{ } \mu\text{m/ms}$ . as previously mentioned, our de-excitation technique is realised using a second IR laser pulse. Such a laser defines a volume in which the de-excitation process is efficient, which we call  $V_{Dep}$ . For the sake of simplicity we can consider  $V_{Dep}$  as a cylinder with the axis on the  $\hat{x}$  direction and radius defined by the waist of the infrared laser:  $w_{IR} = 90 \text{ } \mu\text{m}$ . If Rydberg atoms during the free evolution escape from  $V_{Dep}$  our technique becomes unreliable. Considering that excitations are created principally at the centre of the cloud, in the worst situation, in which the velocity is in the y-z plane, atoms remain in the interaction volume for  $\langle t \rangle \sim \frac{w_{IR}}{\langle v \rangle} \sim 750 \text{ } \mu\text{s}$ , which is more than twice the maximum lifetime expected.

If the 780nm lasers are switched off for too long, the atoms can move out of the cooling region, defined by the overlap of the six trapping lasers, and consequently be lost in the next trapping cycle. In order to prevent significant losses of trapped atoms, we switch off the trapping lasers only for  $t_{free}=1.5 \text{ ms}$  on an experimental cycle of 100 ms. With this timing we see no changes in the steady-state number of MOT atoms.

The last parameter that we must take into account is the mean distance between Rydberg atoms  $\bar{r}$ . The strong dipole-dipole interactions could alter the excited atom's wavefunctions and consequently their lifetimes.

Moreover, since we cannot excite resonantly atoms at distance less than the blockade radius  $\text{Tab}(1.4)$ , with the same assumptions we cannot de-excite them resonantly. Therefore if the excitations are created at a distance comparable with the blockade radius we can expect a loss of de-excitation efficiency during the dynamics. In our experiments we set timings and excitation Rabi frequencies such as to reveal around  $2 \div 3$  atoms, hence considering the detection efficiency of  $\eta = 40\%$  in the experimental volume 5-8 atoms are excited. Approximating a uniform distribution of Rydberg excitations inside the excitation volume (2.1), the Rydberg density can be calculated as  $\rho_{Ry} = \frac{N_{exc}}{V_{exc}}$  and consequently we determine the mean distance

as  $\bar{r} = \rho^{-1/3} \sim 100 \mu\text{m}$ . Such a mean distance is much bigger than the  $r_b$  for the 105S Rydberg state Tab(1.4), that is the highest level investigated. So, we can argue that with these numbers of excitations interaction processes can be neglected.

## 3.2 De-excitation techniques

In my thesis work, I studied the lifetime of different angular momenta Rydberg states. As explained previously a state-selective detection is necessary to distinguish different states close in energy. Moreover working with very high-lying Rydberg states, standard techniques to selectively detect different levels such as state-selective field ionisation [32] become unfeasible. In state-selective field ionisation a ramp of electric field is used to ionise levels with different ionisation thresholds at different times, and the differences in the time of arrival at the channeltron are used to distinguish different energy states.

With increasing principal quantum number, the energy differences between nearby levels becomes smaller and smaller resulting in similar ionisation thresholds of different states and indistinguishable arrival times [10].

### 3.2.1 De-excitation for S-D states

As explained in section 2.3, we have the possibility to change the IR laser frequency using the cat-eye scheme. In particular, if we call  $\nu_0$  the frequency of the laser, passing twice through the AOM it becomes  $\nu_0 + 2\nu_{RF}$ .

For the excitation pulse, we use  $\nu_{RF} = 57 \text{ MHz}$  and we set  $\nu_0$  in such a way that:

$$\nu_{Blue} + \nu_0 + 2\nu_{RF} = \frac{E_{RyS} - E_{GND}}{h} \quad \rightarrow \quad \nu_0 + 2\nu_{RF} = \frac{E_{RyS} - E_{6P}}{h} - \delta_{Blue} \quad (3.1)$$

Right after this pulse, keeping the same  $\nu_0$ , we increase  $\nu_{RF}$  by about  $\delta_{Blue}/2$  and we perform a depump frequency scan, finding the radiofrequency which realises the condition:

$$\nu_0 + 2\nu'_{RF} = \frac{E_{RyS} - E_{6P}}{h} \quad (3.2)$$

as depicted in Fig(2.4)

Using a  $5 \mu\text{s}$  IR pulse only the excited atoms in the target state are coupled to  $|6P_{3/2}\rangle$  state. The decay rate of the lower state to ground state is  $\Gamma_{6P} \sim 8.3 \text{ MHz}$  which is about 10 times greater than the Rabi frequency for the de-exciting processes. This means that each de-excited atom rapidly decays to ground state.

For the second pulse, we increase the IR power to 60 mW, reaching a depump efficiency  $\xi \sim 95\%$ . This technique will be crucial in the lifetime protocol.

Nothing changes in the frequency settings for D states but a lower infrared power is necessary otherwise a strong power broadening is caused. This is due to the fact that the dipole matrix element  $d_{nD-6P} > d_{nS-6P}$  causes a higher Rabi frequency.

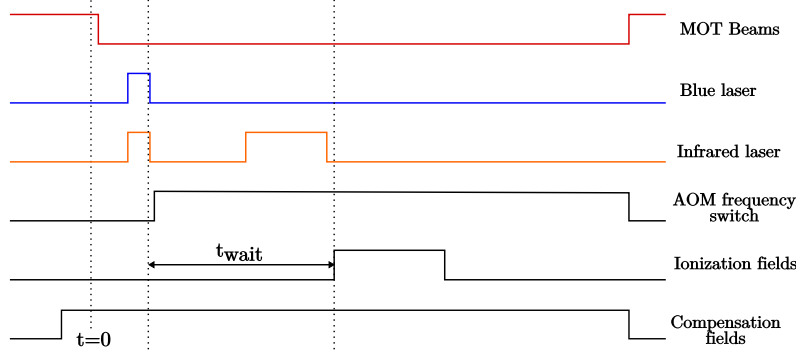


Figure 3.1: Complete timings scheme of our experiments. The beginning of the cycle is indicated with  $t = 0$ . In the fifth line the definition of  $t_{wait}$  is clarified. All the relevant TTL pulses involved in the experiments are depicted. During the measurements in which we do not de-excite atoms, the AOM frequency switch (fourth line) is turned off. In the P-state measurements another TTL pulse which controls the microwave switch is created and it is timed to overlap the third line.

### 3.3 S-D states lifetime protocol

The apparatus and the excitation technique needed for this measurement have been already discussed in the previous chapters.

We excite a population in the desired target Rydberg state and we leave it free to evolve. After a variable period of time  $t_{wait}$  we apply the ionisation pulses and all the excited atoms with principal quantum number greater than 60 are field ionised ( $N_{ens}(t)$ ). The measured number of Rydberg atoms is the sum of atoms in the target state and the number of atoms migrated to other levels through BBR induced transitions. We call this quantity the *Ensemble*.

In a second measurement we repeat the same steps, but  $5 \mu s$  before ionisation we operate a depump laser pulse which de-excites almost all the population that still is in the target state ( $N_{supp}(t)$ ). In this way we measure all the excited atoms except for the atoms in the target state: this quantity is called *Support*.

From the difference of the two measurements, we obtain the population in the target state  $N_{tar}(t) = N_{ens}(t) - N_{supp}(t)$ . Repeating this procedure for different  $t_{wait}$  we measure the

dynamics for the three populations defined above. A typical measurement of the lifetime by using this protocol is shown in Fig(3.4). For the target and the support curves, we limit the observation up to  $t_{wait} = 1.5$  ms whereas for the ensemble we arrive at  $t_{wait} = 6$  ms. The shorter observation time for the two curves is chosen because, the longer the waiting time, the higher the probability to exit the volume  $V_{Dep}$  for an atom. Hence, we can expect a loss of efficiency for the depump pulse at long times. Moreover, as already exposed in section 2.3, 1.5 ms after the excitation we turn off the compensation fields, causing a Stark shift to the excited Rydberg states. So after 1.5 ms the depump laser is detuned to the intermediate 6P state and another loss of efficiency is expected.

This limitation is not a problem for our measurement, in fact, all the investigated lifetimes are below 400 microseconds and an observation time of 1.5 millisecond is enough to include the whole evolution for each Rydberg state.

The expected *Ensemble* lifetimes are longer than the target lifetimes and reach the millisecond order for principal quantum numbers above 90. Nevertheless, for this measurement, we are not constrained by a second laser pulse and the Stark shift caused by the shutdown of the compensation fields does not affect the measurements. Moreover, we do not need the excited atoms to still be in  $V_{Dep}$  because the ionisation process remains efficient also for atoms that have moved outside the MOT region by a few millimeters. For these reasons we can observe this population for a longer time.

For each  $t_{wait}$  we repeat the same measurement 100 times, the reported number of atoms is the average value and the reported error is calculated as the standard deviation divided by the square root of the number of iterations.

We fit the ensemble and the target curves with a single exponential function, by imposing the vertical offset to zero for  $t_{wait} \rightarrow \infty$  to evaluate the decay timescale.

As discussed in chapter 1, once the atoms are transferred by BBR, repopulation processes can occur. Such a repopulation deviates the behaviour of the target curve from an ideal single exponential decay. These deviations become more appreciable for long times when almost all the states are transferred. The ensemble population is not affected by BBR transitions but the single exponential fit is again an approximation because its decay depends on a combination of the spontaneous decay rates of all the atoms present in the sample.

In order to avoid confusion, we now define more clearly what we mean by "lifetime" in the present context. The rigorous definition of lifetime is derived from the equation:

$$\frac{dN(t)}{dt} = -\frac{1}{\tau}N(t)$$

In our case each state is coupled with all the others and, in terms of rate equations, the system is controlled by:

$$\frac{dN_n(t)}{dt} = -\left(\Gamma_n^{SP} - \sum_{n'} \Gamma_{nn'}^{BBR}\right)N_n(t) + \sum_{n'} \Gamma_{n'n}^{BBR}N_{n'}(t)$$

$$\frac{dN_{Ens}(t)}{dt} = \sum_n \frac{dN_n(t)}{dt}$$

These considerations mean that a precise definition of the lifetime is impossible but, from the analysis made in chapter 1, the repopulation processes are expected to cause small deviations from exponential decay.

In conclusion, in the following discussions with the word "lifetime" we refer to *decay timescale*.

### 3.3.1 Results and discussion for S states

We have measured both lifetimes for different principal quantum numbers spanning from  $n=60$  to  $n=105$ , and the results are shown in Fig.(3.2).

Observing the target lifetimes, the experimental data are in good agreement with theoretical predictions for principal quantum number from 60 to 68 and from 74 to 88. A pronounced deviation appears in the range from 90 to 100, whereas, a small deviation appears in the range from 68 to 74. Furthermore, the ensemble data are in good agreement with theoretical predictions before  $n = 75$ , and above this value it seems generally lower by about 20%. From those different behaviours we can understand that the lower target lifetimes do not correspond to lower ensemble lifetime. In other words we can suppose that the increased losses from target state are not due to greater spontaneous decay rates or errors during the detection protocol, but to enhanced induced transition rates to nearby levels.

The neighbouring, dipole allowed, transition frequencies in the deviation ranges are reported in Tab.(3.1). Considering the states around  $n=90$  we see that the transition frequencies are about 4-5 Ghz, similar to the Wi-Fi or radars signals. To ensure that this effect is not due to other external signals, we built a Faraday cage, made by aluminium foils, around the whole experimental apparatus. We used the microwave set-up described in section 2.2.2 to verify the shielding efficiency. We use microwaves at 4.6 GHz to couple the  $|91S_{1/2}\rangle$  state with the  $|90P_{3/2}\rangle$  state. Measuring the Autler Towns splitting (1.30) both with and without the Faraday cage we extracted the microwave intensity at the MOT position in both conditions, deducing a power attenuation factor of about 4. If the deviations are caused by the interaction with external radiations, using this shielding cage we expect to see a smaller effect, so better

$n$	$\nu_{nS \rightarrow nP_{3/2}}$	$\nu_{nS \rightarrow nP_{1/2}}$	$\nu_{nS \rightarrow n-1P_{3/2}}$	$\nu_{nS \rightarrow n-1P_{1/2}}$
69	11.14	10.85	11.89	12.2
70	10.65	10.37	11.36	11.66
71	10.19	9.92	10.87	11.15
72	9.76	9.50	10.40	10.67
73	9.34	9.09	9.96	10.22
74	8.96	8.72	9.54	9.79
90	4.87	4.74	5.17	5.30
91	4.71	4.58	4.99	5.12
92	4.55	4.43	4.83	4.95
93	4.40	4.28	4.67	4.79
94	4.26	4.14	4.51	4.63
95	4.12	4.01	4.37	4.48
96	3.99	3.88	4.23	4.34

Table 3.1: Transition frequencies from  $nS$  state to its neighbouring P levels for  $n$  in the depletion region. All the transition frequencies are expressed in GHz and calculated using the ARC function `atom.getTransitionFrequency()`

agreement with theory.

We repeated the lifetime measurement, for 91S state, obtaining the same results within experimental errors. Therefore, reasonably, we can affirm that these deviations are not caused by external signals.

We suppose, as mentioned in section 1.2.1, an alteration of the density of modes of the electromagnetic field present inside the vacuum cell due to the geometrical dimensions of the experimental set-up surrounding the MOT. To understand if such hypothesis is plausible we must relate the deviations from theory to the transition frequencies.

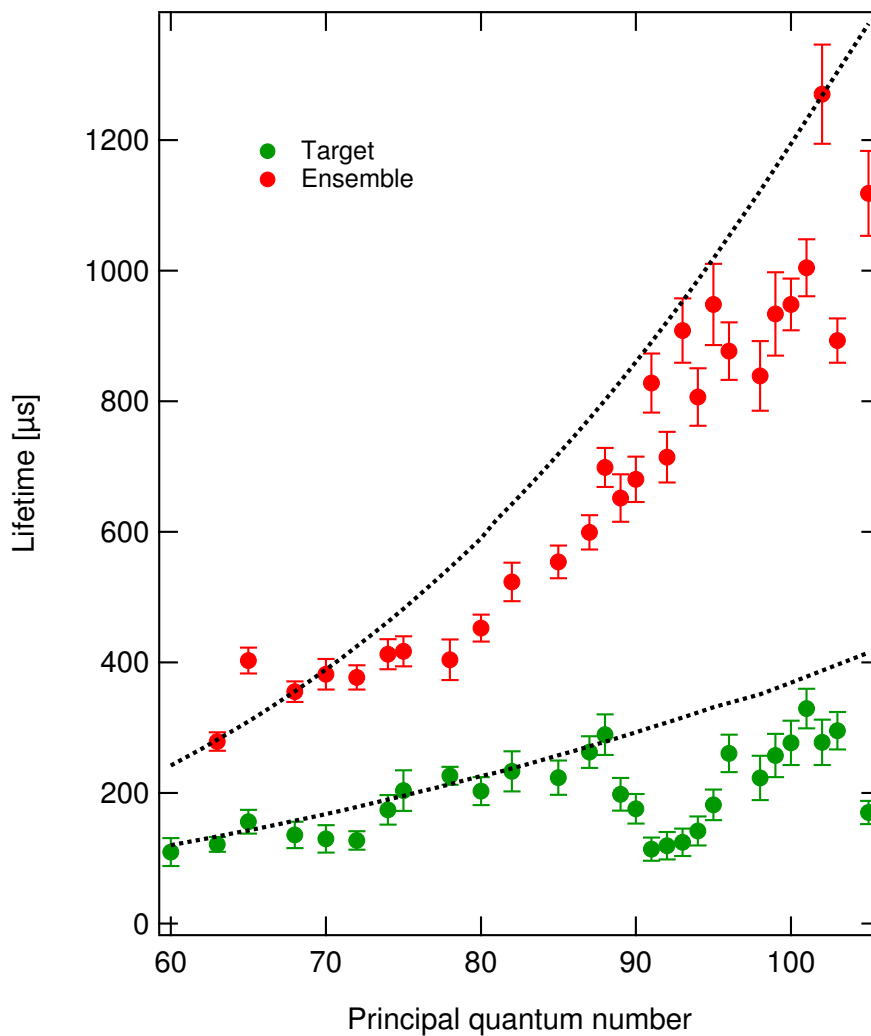


Figure 3.2: Target and ensemble lifetime for S states. The dotted line superposed to the experimental data is the theoretical prediction made by I.I. Beterov [33].

### 3.3.2 De-excitation for P states

I turn now to the discussion of the de-excitation technique for P Rydberg states. As in the S states technique, we want to couple the target state with an intermediate state of rapid decay rate. The two possible low-lying states we could use to depump directly a nP state are  $|6S_{1/2}\rangle$  state and  $|5D_{5/2}\rangle$  state, which have transition wavelengths respectively of about  $\lambda_{nP \rightarrow 5D} = 1250$  nm and  $\lambda_{nP \rightarrow 6S} = 738$  nm.

The same resonant IR laser pulse used before is unfeasible with the cat-eye scheme because the required changes in laser frequency are too large. However, we can use a combination of the laser and the microwave to couple the P Rydberg state with the  $|6P_{3/2}\rangle$  through a 2-photon transition, again, shifting the IR frequency by  $\delta_{Blue}$ . We use the maximum IR power available with our apparatus of about  $P_{IR} = 60$  mW whereas, for the MW, we use the same power used during the excitation. Fig.(3.3) shows a schematic representation of the RF values used during the different stages.

This process is not efficient as the single photon one, in fact, we increase the duration of the depumping pulse to  $\tau_{Dep} = 10$   $\mu$ s and, in spite of the longer pulse, we obtain efficiencies of  $\xi_{dep} = 45 \div 90\%$ .

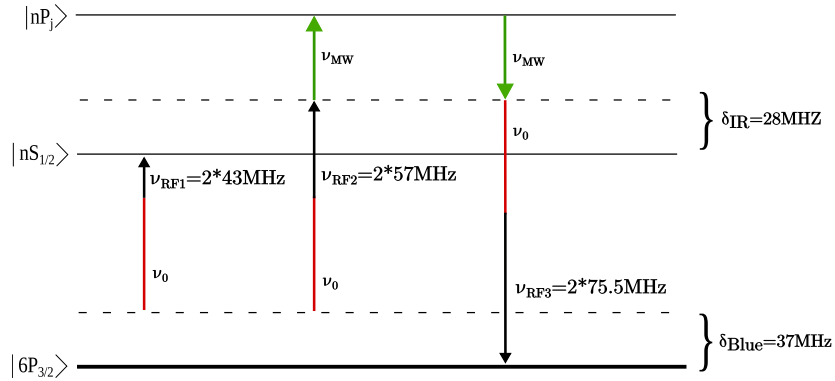


Figure 3.3: P excitation and de-excitation scheme. First, driving the AOM with 43 MHz, we find the resonant  $\nu_0$ . In a second stage we increase  $\nu_{RF}$  to 57 MHz and we set the resonant microwave. Finally using both the microwave and the IR pulse and driving the AOM with 75.5 MHz we are resonant with the lower intermediate state.

If we want to observe a lifetime on the  $\tau$  timescale, the duration of the depump pulse has to be at least an order of magnitude lower, otherwise a significant part of the evolution is integrated out. Considering the lowest expected lifetime in our experiments to be on the order of 100 microseconds, we chose  $\tau_{Dep} = 10$   $\mu$ s in order to have  $\frac{\tau_{Dep}}{\tau_{Ry}} < 10\%$  for all the investigated Rydberg states. This lack of efficiency is due to a low two-photon Rabi frequency,

but as already exposed in section 2.2.2, we cannot increase the microwave power if we want to preserve unmixed states.

To ensure that the longer depump time and the lower efficiency do not affect the measured lifetime we repeat an 69S lifetime measurement increasing  $\tau_{Dep}$  to 10  $\mu\text{s}$  and artificially reducing the de-excitation efficiency to 60%, lowering the laser power after the excitation. The measured target and ensemble lifetimes with the standard protocol were respectively:  $\tau_{tar}^{\text{Standard}} = 105 \pm 13 \mu\text{s}$  and  $\tau_{ens}^{\text{Standard}} = 428 \pm 18 \mu\text{s}$ . With lower depump efficiency we obtained:  $\tau_{tar}^{\text{Ineff}} 106 \pm 19 \mu\text{s}$  and  $\tau_{ens}^{\text{Ineff}} 413 \pm 18 \mu\text{s}$ . These values are in agreement both for the target and the ensemble. This is a first confirmation that we can exploit this technique to measure P-state lifetimes.

Another validation of the independence of the measured lifetimes with respect to low de-excitation efficiencies will be outlined in chapter 4, through a simulation of the processes above explained.

### 3.4 P states lifetime protocol

In order to confirm the fact that those deviations are due to enhanced density of modes of blackbody radiation we decided to repeat the same lifetime measurements for states with angular momentum 1, known as P states.

The P states having more allowed transitions (to S and D states) involve more frequencies. We can expect that in different ranges of principal quantum number the suspected enhanced frequencies of Tab(3.1) appear as neighbouring transition to D states causing other deviations from theory. The comparison of the two lifetime plots can bring us to a better understanding of the enhanced transitions.

The protocol for the measurements of the P states lifetime is similar to the S protocol: we excite a population in the desired Rydberg state through a three-photon transition and we leave it free to evolve interacting with BBR. After a certain time, we field ionise the remaining excited states and we measure them ( $N_{ens}(t)$ ).

This time in the second measurement, after repeating the same steps, 10 microseconds before field ionisation we apply the two-photon de-excitation pulse, driving only a fraction of the target state to ground. As shown in the previous section the efficiency of two-photon depump processes is limited by the microwave intensity. We call this quantity *support* although it contains a small population in the target state  $N'_{supp}(t) = N_{supp}(t) + (1 - \xi_{dep})N_{tar}(t)$ .

Finally, from the difference between the two, we obtain the number of depumped states which we consider as the population in the target state  $\xi_{dep}N_{tar}(t) = N_{ens}(t) - N'_{supp}(t)$ .

Repeating the same procedure for different waiting times we trace the evolution curves for

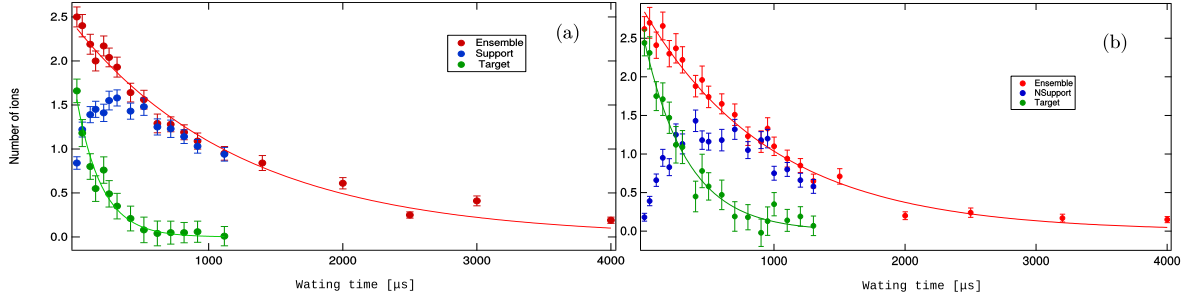


Figure 3.4: (a) Lifetime measurement of  $|97P_{3/2}\rangle$  state. Red, blue and green dots represent respectively the experimental values of ensemble, support and target. The superposed lines are the exponential fit for the target and the ensemble. The difference from the first ensemble data to the target one is due to the low depump efficiency, that in this case is about 68%. The obtained lifetimes are:  $\tau_{97P} = 187 \pm 25 \mu\text{s}$  and  $\tau_{Ens(97P)} = 1262 \pm 46 \mu\text{s}$ . (b) Lifetime measurement of  $|101S_{1/2}\rangle$  state. The colours are the same of (a). The obtained lifetimes are:  $\tau_{101S} = 313 \pm 27 \mu\text{s}$  and  $\tau_{Ens(101S)} = 981 \pm 38 \mu\text{s}$

the ensemble, the support, and the target as depicted in Fig.(3.4).

The same care is taken, as in the S state measurement, for the observation time of the target and the support to be limited up to 1.5ms.

An exponential fit without constant term is performed for each target and ensemble curve where, again, each point is averaged over 100 iterations of the same measurement as for the S-D values.

### 3.4.1 Results and discussion for P states

Our microwave generator can work at a maximum frequency of 13.5 GHz and this limit our possibility to excite states below the 66P. We have measured the target and the ensemble lifetimes for principal quantum numbers in the range from  $n=66$  to  $n=100$ . Contrary to the S states, the P states have two possible total angular momentum values ( $J = 1/2$  and  $J = 3/2$ ). Theoretically the lifetime difference between the two sublevels is smaller than our experimental error. The data shown in Fig.(3.5) are a mixture of different angular momenta randomly chosen. We use darker filled dots for  $J = 1/2$  data and lighter empty dots for  $J = 3/2$  data. Furthermore we measured both total angular momentum lifetimes for the 95P and 88P, obtaining values compatible within the experimental error.

As expected from the S results Fig(3.2), a huge deviation from theoretical predictions appears in the range around 90, but it seems enlarged, whereas the small deviation in the range around 70 is similar to the S one. A new significant deviation appears in the range from 76 to 80.

The results for the ensemble are in a good agreement with theoretical predictions, except for the region around 92 that appears with a lower lifetime than expected.

Calculating the theoretical neighbouring transition frequencies to D states for principal quantum numbers in the new depletion range, Tab.(3.2), we can see that there is a peculiar coincidence of frequencies in the suspected ranges with enhanced density of modes, defined in the previous section. Such a combination of enhanced transition rates implies a lifetime drop, as observed experimentally.

From those results we demonstrate a correlation between lifetime lower than expected and first neighbour transition frequencies, highlighting that at MOT position the electromagnetic spectrum differs from Planck's formula principally in the regions around 4.5 GHz and 11 GHz.

$n$	$\nu_{nP_{1/2} \rightarrow n-1D_{3/2}}$	$\nu_{nP_{3/2} \rightarrow n-1D_{3/2}}$	$\nu_{nP_{3/2} \rightarrow n-1D_{5/2}}$
76	5.09	4.87	4.89
77	4.88	4.67	4.7
78	4.69	4.49	4.51
79	4.51	4.32	4.34
80	4.34	4.15	4.17
$n$	$\nu_{nP_{1/2} \rightarrow n-2D_{3/2}}$	$\nu_{nP_{3/2} \rightarrow n-2D_{3/2}}$	$\nu_{nP_{3/2} \rightarrow n-2D_{5/2}}$
76	11.72	11.92	11.94
77	11.25	11.47	11.44
78	10.81	11.01	10.99
79	10.39	10.58	10.56
80	9.99	10.18	10.15

Table 3.2: P states to D states transition frequencies in the new depression range. Frequency are given in GHz

The enlargement around  $n = 90$  gives us information about frequencies lower than 3 GHz, unexplored with S states. The neighbouring transition frequencies to D states in that range of principal quantum numbers are in fact from 3.3 GHz to 2.0 GHz whereas the minimum transition frequency involved in S state measurements was  $\nu_{105S \rightarrow 105P} \sim 3$  GHz. From those results other deviations can be expected in that range of frequencies. Considering equation (1.12) and using the approximation  $h\nu \ll k_B T$  for  $T = 300$  K and  $\nu$  on the order of few GHz, we can use the Rayleigh-Jeans formula to estimate the intensity of blackbody radiation at the transition frequency in Tab(3.1) as:

$$I(\nu, \Delta\nu) = \int_{\nu_0 - \Delta\nu}^{\nu_0 + \Delta\nu} \frac{2k_B T \nu^2}{c^2} d\nu = \frac{4k_B T}{3c^2} [3\nu_0^2 \Delta\nu + \Delta\nu^3] \quad (3.3)$$

Using for  $\Delta\nu$  a typical transition width of about  $\Delta\nu = 1$  MHz and imposing  $\nu = 4$  GHz we obtain the intensity of  $I(4\text{GHz}, 1\text{MHz}) \sim 0.3$  fW/cm<sup>2</sup>. Since the deviations seen in the experimental data correspond to an enhancement of radiation intensity on the order of fW/cm<sup>2</sup>, clearly we cannot detect them with other standard sensors.

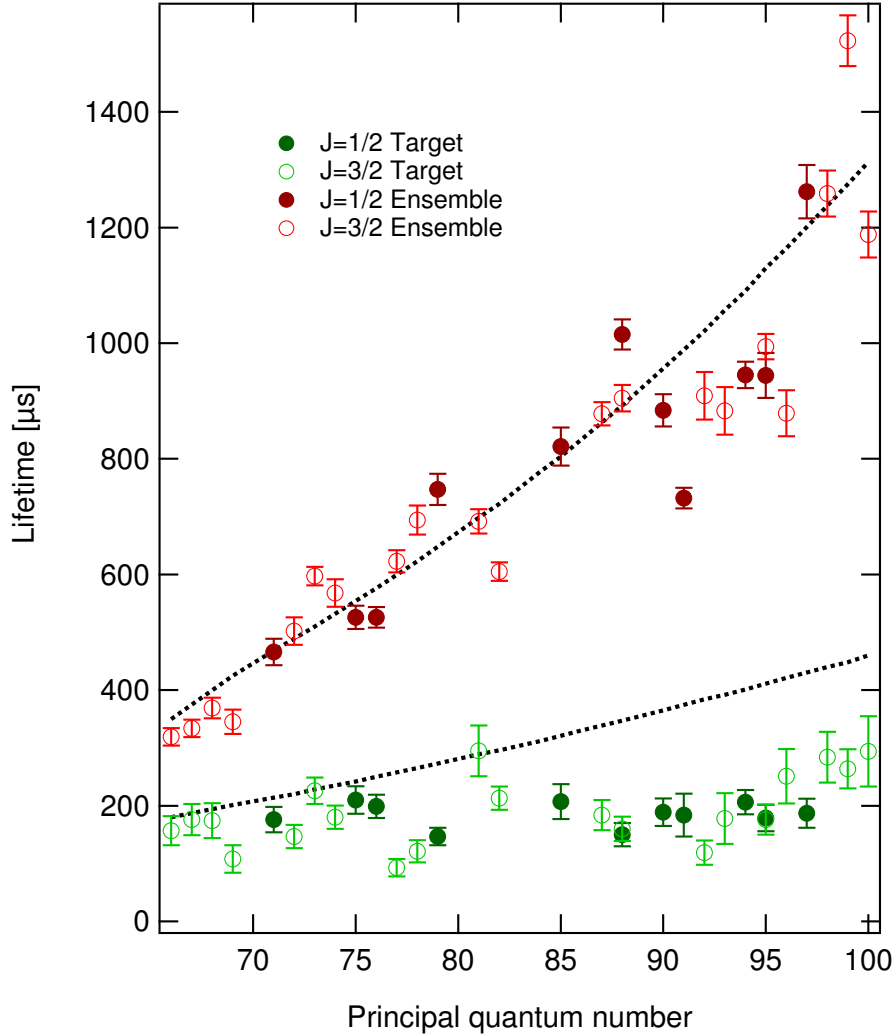


Figure 3.5: Target and ensemble lifetimes of Rydberg P states, the lighter empty dots represent the measured lifetime for states with total angular momentum  $J = 3/2$  and the darker filled dots represent the measured lifetime for  $J = 1/2$  states. For 95P and 88P we measured the lifetimes for both values of J, which are compatible within the experimental error. The dotted line superposed to the experimental data is a theoretical calculation for  $J = 3/2$  states that I simulated, including the repopulation processes, as it will be explained in the next chapter.

### 3.5 Result for D states

To complete our set of data we decided to measure also D state lifetimes to confirm our predictions on the correlation between lower than expected lifetimes and neighbouring transition frequencies. These measurements are now under investigation and I report an incomplete plot that will be completed in future works.

The D states involve again different frequencies in different ranges of principal quantum numbers, so, a better understanding of blackbody spectrum can be achieved comparing the three plots.

Up to now we have measured the lifetime of D states in the range from  $n = 78$  to  $n = 92$  of only  $J=5/2$  sublevels. The results of these measurements are reported in Fig(3.6). The data are not enough to argue something about deviations as seen in S and P states, but a lower lifetime than expected is highlighted for all the principal quantum number considered.

For D states in the regions of principal quantum number investigated we found that for each state there are transitions allowed around 3 GHz, 4.5 GHz or 11 GHz. In light of the previous discussions we can explain such lower lifetimes with the same hypothesis of enhanced transition rates.

### 3.6 Conclusions

This chapter demonstrates that we are able to correctly measure the lifetime of very high-lying Rydberg states with different angular momenta. The results confirm that Rydberg atoms are an optimal sensor to measure extremely small variation of radiation intensity.

The results for S states highlight that several transitions, in the frequency ranges from  $4 \div 5$  GHz and from  $10 \div 12$  GHz have an enhanced rate. The results for P states confirm this finding and show that other deviations at frequencies lower than 3 GHz are expected.

We have excluded the possibility that external signals influence our measurement. Furthermore in light of the care taken to control the experimental conditions we exclude internal effects as interactions between Rydberg states or Stark shifts. Without other sources of disturbance we can argue that inside our vacuum cell we have measured the presence of more thermal photons than expected from Planck's formula.

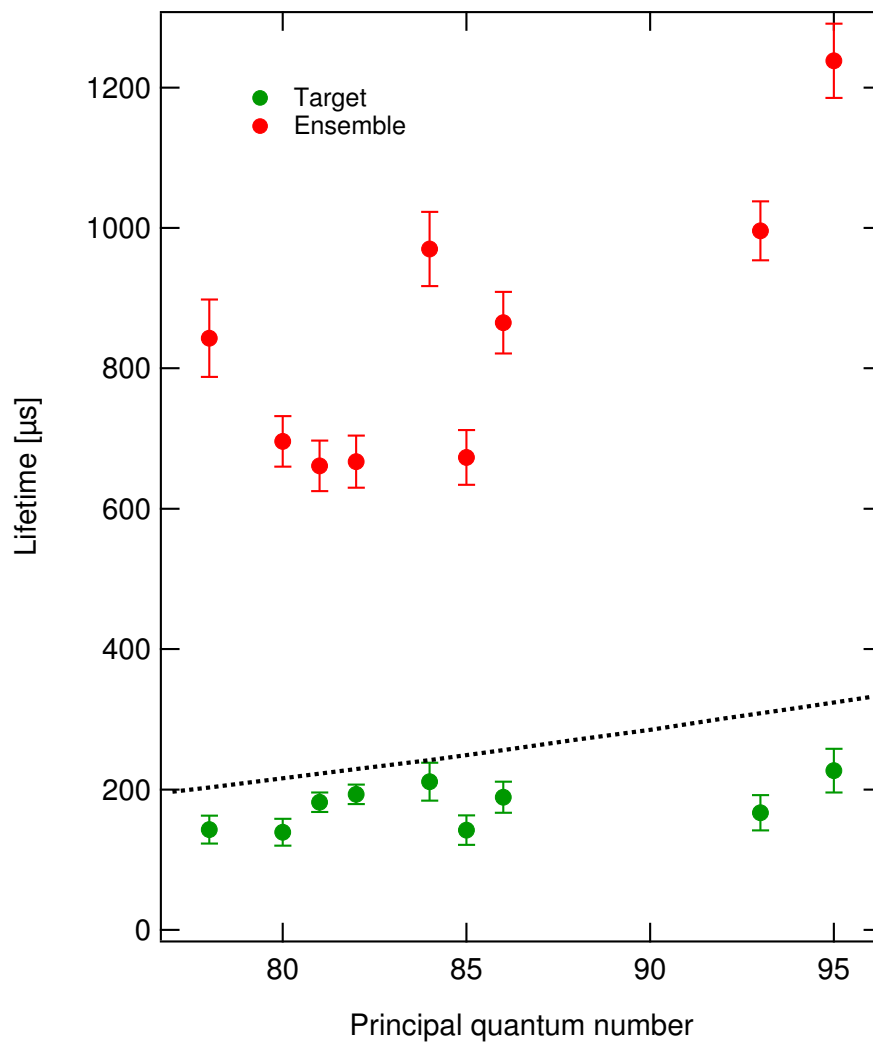


Figure 3.6: Target and ensemble lifetimes of Rydberg D states. Theoretical predictions that include repopulation processes will be calculated in future work. The dotted line is the lifetime calculated with ARC function `atom.getStateLifetime()`.

## Chapter 4

# Simulation of Rydberg dynamics

In this chapter, I will describe the simulations made to analyse the results presented in chapter 3. I will start describing the Python library ARC, the central point of the following sections. Once clarified the basis I will proceed to explain the C program which, exploiting ARC features, simulates the dynamics of a Rydberg atom interacting with BBR.

### 4.1 ARC-Alkali Rydberg Calculator

ARC is an open-source Python library for computing properties of highly-excited Rydberg states of alkali atoms [16]. Moreover it provides a set of built-in functions that are useful to perform single atom and also pair interaction calculations. In the course of my thesis this program was extensively used; for example the Stark maps shown in Fig(2.6) are a diagonalisation of the Hamiltonian in the presence of an electric field, computed using ARC functions. However to calculate the effective Rydberg states lifetime, only a small number of functions provided by this library were used. I want to point out the principal functions necessary for the analysis made:

```
atom.getTransitionFrequency(n,l,j,n',l',j')
```

This function returns the energy difference from  $|n, l, j\rangle$  state to  $|n', l', j'\rangle$  state in Hz. We used it to calculate all the transition frequencies from S to P states we experimentally achieved and to realise the program which will be exposed in the next chapter.

```
atom.getTransitionRate(n,l,j,n',l',j',temperature)
```

As explained in chapter 1 a Rydberg atom undergoes transitions to other states mainly for two reason: spontaneous emission, and coupling with BBR. For both processes we can define

a transition rate. This function returns such rates for a specific transition: as above it takes as inputs the parameters of the starting state  $n,l,j$  and of the state of arrival  $n',l',j'$ , but, to correctly evaluate the rates, it has to include temperature as a parameter.

If the temperature ( $T$ ) is set to zero, it calculates only spontaneous emission rates  $A_{nlj \rightarrow n'l'j'}$  whereas if  $T$  differs from zero it also includes in the result the BBR transition rates, calculated as:

$$\Gamma_{T=0} = \frac{4\omega_{nn'}^3 l_{max}}{3c^3(2l+1)} |\langle nl|r|n'l' \rangle|^2 \quad \Gamma_{T \neq 0} = \Gamma_{T=0} \left( 1 + \frac{1}{\exp(\hbar\omega_{nn'}/k_B T) - 1} \right) \quad (4.1)$$

The notation used is the same of (1.4). I used this function to create a data structure **STATE** in the program described in the next section.

Fig(4.1) shows the calculated transition rates for  $|90S_{1/2}\rangle$  and  $|90P_{3/2}\rangle$  states. As already emphasised in section 1.1, the spontaneous decay rates are appreciable only to low-lying states whereas the BBR induced rates are significant only to energy levels nearby the target states.

`atom.getStateLifetime(n,l,j,temperature, includeLevelsUpTo)`

This function returns the lifetime of the Rydberg state identified with  $n,l,j$ . The temperature is necessary to correctly define the BBR transition rates, and `includeLevelsUpTo` is a parameter that defines the upper state considered in the calculation, typically we use `includeLevelUpTo = n + 20`.

This function performs the sum of all the possible transition rates both spontaneous and BBR induced, and after that, it calculates the lifetime as the inverse of the total transfer rate:

$$\Gamma_{n,l,j} = \sum_{n'=5}^{\text{includeLevelsUpTo}} \sum_{l',j'} \Gamma_{nlj \rightarrow n'l'j'}^{TOT} \quad \rightarrow \quad \tau_{ARC} = \frac{1}{\Gamma_{n,l,j}} \quad (4.2)$$

Here I used  $\Gamma^{TOT} = \Gamma^{BBR} + \Gamma^{SP}$ .

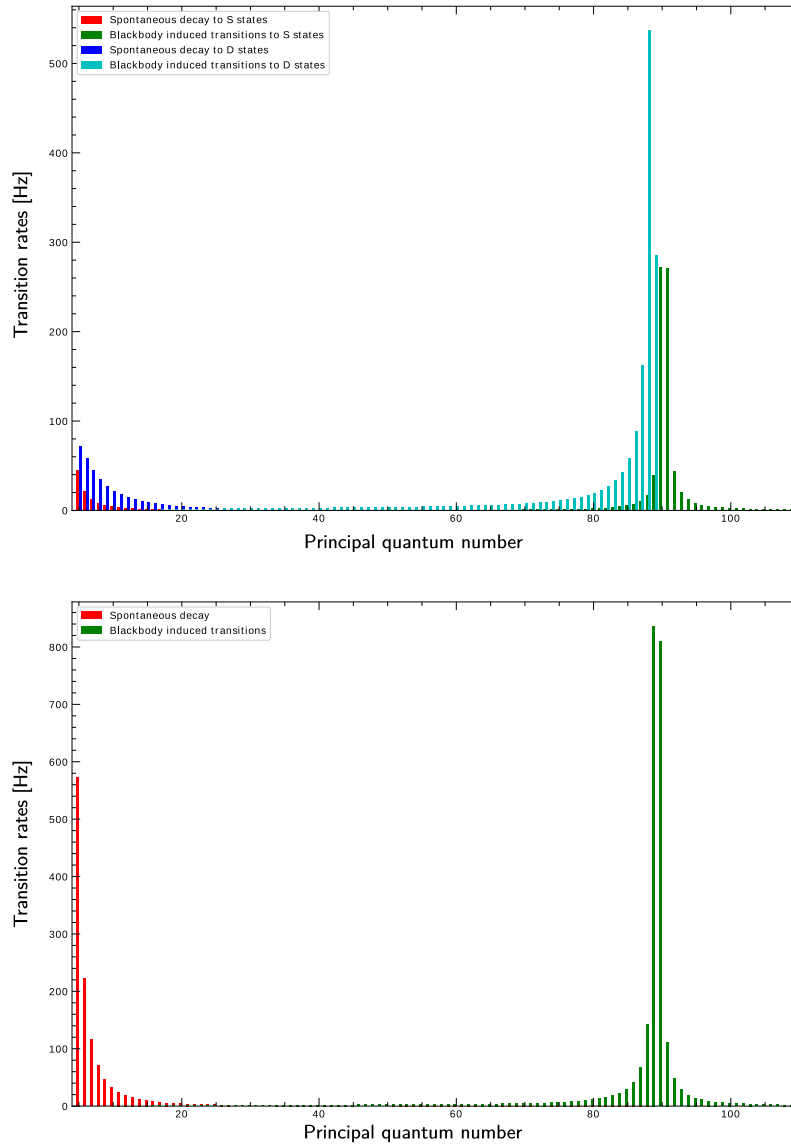


Figure 4.1: Spontaneous and BBR induced transition rates for: (on the top) state  $|90P_{3/2}\rangle$  and (on the bottom) state  $|90S_{1/2}\rangle$ . These rates are computed with the program ARC using the function `atom.getTransitionRate()`. In both cases only the spontaneous decay rate to states close to the ground state is appreciable, whereas, the BBR induced transitions are significant only for states in the neighbourhood of the target state.

## 4.2 Lifetime simulation

As I have already pointed out the actual lifetime of a Rydberg atom differs from (4.2), in which both spontaneous emission and BBR induce transitions are considered, but the processes in which an atom, once transferred to a nearby level, can repopulate the initial state are not taken into account. This phenomenon is the central issue of this section.

Considering all the possible transitions, for the population dynamics of a state  $nlj$  we have:

$$\left\{ \begin{array}{l} \vdots \\ \frac{dN_{nlj}}{dt} = \sum_{n'=5}^{n_{max}} \sum_{l'=l-1}^{l+1} \sum_{j'=l'-1}^{l'+1} \left( \Gamma_{n'l'j' \rightarrow nlj}^{TOT} N_{n'l'j'}(t) - \Gamma_{nlj \rightarrow n'l'j'}^{TOT} N_{nlj}(t) \right) \\ \vdots \\ \frac{dN_{5S_{1/2}}}{dt} = \sum_{n'=5}^{n_{max}} \sum_{j'=1/2}^{3/2} \Gamma_{n'Pj' \rightarrow 5S_{1/2}}^{TOT} N_{n'Pj'}(t) \end{array} \right. \quad (4.3)$$

The  $n$ ,  $l$  and  $j$  parameters run over all the possible values and  $N_{nlj}(t)$  is the population in the state  $n$ ,  $l$ ,  $j$  at the time  $t$ . I have considered that an atom decayed to the ground state cannot escape from there. The initial conditions are:

$$\begin{cases} N_{nlj}(0) = N_0 & \text{if } n = n_{target}; l = l_{target}; j = j_{target} \\ N_{nlj}(0) = 0 & \text{otherwise} \end{cases}$$

The analytical solution of such a system, evidently, is prohibitively difficult and a numerical resolution seems to be a simpler strategy.

### 4.2.1 Approximations

To start facing the calculation of the decay timescale of a Rydberg state, we need some physical considerations or constraints that simplify it as much as possible.

For S state we have theoretical predictions which include repopulation processes made by I.I. Beterov [33]. My program emulates his calculations and was used principally for P states simulations.

The first consideration is about the range of principal quantum numbers experimentally investigated, that are from 66 to 100. Starting from 100P state the probability of reaching a state with  $n$  above 110 through a BBR transition and then, from that state, returning back to the 100P during the evolution is extremely low. For this reason I decided to fix  $n_{max} = 110$ .

Looking at 66P as the lowest state investigated, with the same assumptions, I chose as lower bound for the principal quantum numbers used in the simulations  $n=59$ . I considered each state with  $5 < n < 59$  as a non-Rydberg state, more precisely, I defined a "ground" state representing any non-Rydberg state. In order to take into account all the possible decay processes, the rate to this state was defined as the sum of the rates to levels with  $5 < n < 59$ . This condition is important because it simulates our detection system that is not able to detect states with principal quantum number lower than 60.

The final constraint imposed is a boundary condition on  $l$ . A jump of three angular momenta needs three consecutive BBR induced transitions each one to a state with higher angular momentum. Therefore to repopulate the target state, at least six BBR induced transitions must happen. Such a process has insignificant probability and can be excluded in the simulation. With the aim of calculating the lifetime of S and P state, only angular momentums lower than 4 were considered. In future works this program will be modified to include also G states to perform correctly D states simulations.

The goodness of the results using these approximations will be verified in section 4.2.3.

#### 4.2.2 The core of the simulation program

Once an atom is excited, at each moment during its evolution, it can make a transition to other Rydberg states or decay to a low-lying state through spontaneous emission. By way of an analogy, we can describe this evolution as a kind of damped random walk in energy and angular momentum spaces, where each step of its evolution is weighted proportionally to the relative transition rate.

I realised a program in C language using ARC as a support to correctly define the transition rates. Each state considered is defined with a structure `STATE` which is composed of:

- three quantum numbers  $n, l, j$ , respectively the principal quantum number, the angular momentum and the total angular momentum that define the quantum state.
- A sequence of pairs  $[\Gamma_{nlj \rightarrow n'l'j'}, \&s_{n'l'j'}]$  in which the first element is the total transfer rate from  $nlj$  state to  $n'l'j'$  state and the second element is the memory location of state  $n'l'j'$ . For the ground state I defined  $\Gamma_{nlj}^{\text{GND}} = \left( \sum_{n'=5}^{n'=59} \sum_{l',j'} \Gamma_{nlj \rightarrow n'l'j'} \right)$ . All these rates are calculated with the ARC built-in function `atom.getTransitionRates()`
- An identifier `sn.l.j` to name the state, for example  $|90P_{3/2}\rangle$  state is represented by `s90.1.1` whereas  $|90P_{1/2}\rangle$  state is represented by `s90.1.0`. The last number of the identifier is the integer part of the total angular momentum.

Upon starting the program, it requires: the three quantum numbers of the state we want to excite  $n, l, j$ , the number of excited atoms `N_exc`, the number of iterations we want to perform `ITER`, the final observation time `TTOT`, and the number of points `NPOINT` for which we want to count the remaining atoms.

A list of `N_exc` states `STATE sn_l_j` is created and each state is left free to evolve from  $t=0$  to  $t=TTOT$ .

At regular intervals  $\frac{TTOT}{NPOINTS}$  a function `count()` checks the total number of "atoms" in the list (Ensemble) and another function `countTarget(nlj)` checks the number of "atoms" that still are in the target state. `countTarget()` can be used also for the observation of the population in other states in order to study the ensemble composition. This procedure is repeated `ITER` times, then, the mean and standard deviation of the results are calculated. If we consider a short enough time step  $t_{step}$ , i.e. the sum of all the transition rates times  $t_{step}$  is:

$$\left( \sum_{n'l'j'} \Gamma_{nlj \rightarrow n'l'j'} \right) t_{step} \ll 1 \quad (4.4)$$

we can define the probability of a certain transition in that time step as:

$$P_{nlj \rightarrow n'l'j'} = \Gamma_{nlj \rightarrow n'l'j'} t_{step} \quad (4.5)$$

Considering that the lowest expected lifetime is about  $\tau_{min} \sim 100 \mu\text{s}$ , which corresponds to  $\Gamma_{max} = \frac{1}{\tau_{min}} \sim 10 \text{ kHz}$ , using  $t_{step} = 50 \text{ ns}$  we have  $\Gamma_{max} t_{step} = 5 \times 10^{-4} \ll 1$  respecting (4.4). The population dynamics of each state is simulated probabilistically, by means of a function called `evolve(STATO *s)`, described in appendix (B).

Finally, the program writes on an external file the results for the averaged populations and the corresponding observing times. The outcomes are fitted with a single exponential function in the same way as the experimental data to maintain a coherent lifetime definition.

A more detailed description of the program that includes the relevant parts of the script will be presented in appendix (B).

### 4.2.3 Result for S and P states and quality check

In order to verify the validity of my approximations, I ran the program using a  $|90S_{1/2}\rangle$  state as starting state counting the number of atoms in each state. To ensure statistical validity I used `ITER=106`. A plot of the ensemble population at different times is reported in Fig.(4.2). At first, we can observe clearly the behaviour of a Rydberg state: from the populated target, the excitation spreads out in energy and angular momentum space. At  $t_{wait} = 270 \mu\text{s}$  a sizeable population is transferred to the neighbouring P states, and at  $t_{wait} = 990 \mu\text{s}$  the

number of atoms in these states becomes greater than the target state population.

Turning to the discussion about the validity of my approximations, we can see that the evolution of the state is principally limited to the nearest 6 levels  $n' = n \pm 1, \pm 2, \pm 3$ , and only a small fraction of the initial population ( $< 1\%$ ) is transferred to the states with  $n' = n \pm 4$  for very long times. This means that, limiting the calculation from  $n = 66$  to  $n = 100$  the range of states taken into account is enough to calculate correctly both the target and ensemble lifetime.

The population transferred to states with angular momentum 3 is only an extremely small fraction and again for times longer than 1 ms. As a consequence they are not relevant to the ensemble lifetime estimation. Moreover for the P states the fact that I do not consider G states has not significantly influenced the outcomes.

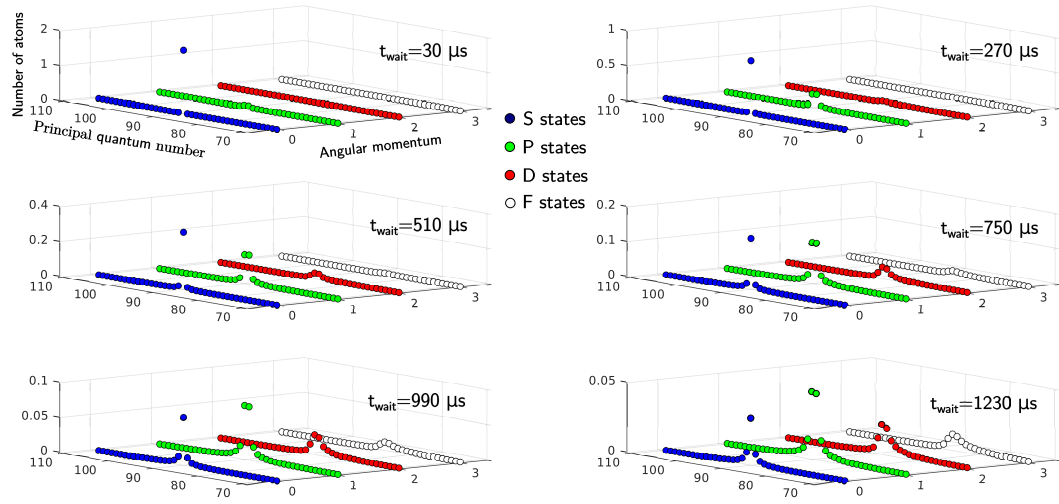


Figure 4.2: Time evolution of the state 90S. In each graph the calculated mean number of excitations is shown for different principal quantum numbers and angular momenta: in blue S states, in green P states, in red D states and in white F states. The results are averaged over  $10^6$  iterations. The axes of each plot are the same as those for  $t_{wait} = 30 \mu s$ , in particular on the vertical axis the mean number of atoms is plotted, on the x axis the principal quantum number and on the y axis the angular momentum. The results for same principal quantum number and angular momentum but different total angular momentum are summed.

For the calculation of P states lifetimes I used  $TTOT = 1.5ms$  divided in  $NPUNTI = 60$ ,  $Nexc = 10$  and  $ITER = 10000$ , obtaining data for the whole range of principal quantum numbers from 66 to 100. The calculations were done only for  $J = 3/2$  states. The results are plotted

in Fig(3.5) in the previous chapter.

To evaluate the effects of repopulation I compared my simulated data based on the equation (4.3) with the lifetime computed by the ARC built-in function `atom.getStateLifetime()` (4.2). From this comparison we can define the *repopulation rate* as the difference of total transfer rates, i.e. the inverse of the calculated lifetime:

$$\gamma_{Rep} = \frac{1}{\tau_{ARC}} - \frac{1}{\tau_{Me}} \quad (4.6)$$

This quantity accounts for the all the transitions from BBR populated support states to the target state.

nP <sub>3/2</sub>	$\tau_{ARC}$ [ $\mu$ s]	$\tau_{Me}$ [ $\mu$ s]	Diff[%]	$\gamma_{Rep}$ [Hz]
71	200	214	6.4	320
75	226	242	6.4	283
81	269	289	7.0	260
86	307	330	7.1	231
92	356	384	7.4	190
99	418	448	6.7	160

Table 4.1: Comparison of lifetime calculated with ARC function, that does not take into account repopulation processes, and data simulated with my program. "Diff" is defined as  $\text{Diff} = 100 \frac{\tau_{Me} - \tau_{ARC}}{\tau_{Me}}$  and  $\gamma_{Rep}$  values are calculated with equation (4.6)

My program returns lifetime values higher than those obtained using ARC by about  $6 \div 7\%$ . As predicted from eq (1.11) the effect of repopulation is not a drastic alteration of the decay dynamics but only a slight change in the decay timescale. Nevertheless these little corrections are important to have precise theoretical predictions with which to compare the experimental data.

#### 4.2.4 Simulation of mixture excitation

As explained in chapter (2), during the three-photon excitations, if a too intense microwave radiation is used, we cause the mixing of the Rydberg S state, which we use as second intermediate state, and the target P state. After the excitation pulse, the dressed state is projected onto the bare states and the sample, which we observe the evolution of, is the mixture of these states.

In this section I discuss the possible deviations of the measured lifetime from theoretical predictions in such a mixture of S and P states.

To this end, I added a new set of required parameters representing the second excited state  $n1, l1, j1$  and the population in that state  $N\_exc1$ . When the program starts, a list is created with  $N\_exc$  states  $STATE\ sn1\_l\_j$  and with  $N\_exc1$  states  $STATE\ sn1\_l1\_j1$ , the remaining part of the program has not been changed. In such a situation, having a population in the nearest S state at  $t = 0$ , we can expect two effects: an increase in the measured target lifetime due to stronger repopulation processes and a shorter ensemble lifetime, due to higher spontaneous decay rates for S states.

Fig(4.3) shows both the ensemble and target lifetimes for  $|85P_{3/2}\rangle$  state together with  $|85S_{1/2}\rangle$  state for different initial compositions. Each point is calculated with  $ITER= 10000$  and  $N\_excP= f_P/10$  and  $N\_excS= 10 - f_P/10$ , where  $f_P$  is the *P-state fraction* reported in the bottom axis of the plots.

Simulating such dynamics we can see that the behaviours of ensemble and target lifetime agree with those shown above. The ensemble lifetime decreases by about 6% when the population goes from a complete P state to a half populated S state whereas the target lifetime increases by 13%.

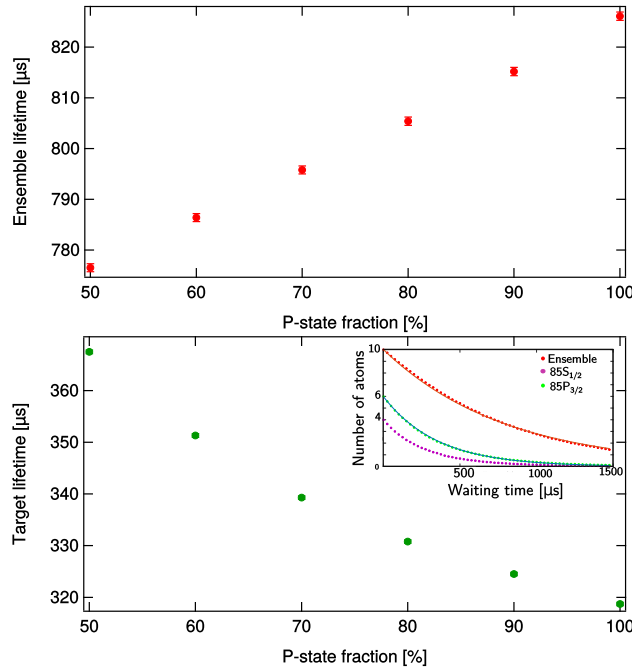


Figure 4.3: The upper graph shows the simulated ensemble lifetime for different initial P state fractions, whereas the lower plot is the simulated target lifetime as a function of the same P state fraction. The inset shows the simulation of an excitation of  $85P_{3/2}$  and  $85S_{3/2}$ . This plot refers to an initial population composed of 60% of P state and of 40% of S state.

These results could also serve as an explanation for the lower ensemble lifetimes measured in the range from 90P to 96P Fig(3.5). In this range of principal quantum numbers we expect the transition rates to neighbouring S states to be increased. In such a situation, although our excitation process is correct, the nearby S states are populated faster than expected leading to a shorter ensemble lifetime.

#### 4.2.5 Simulation of inefficient de-excitation

To conclude this section, I proceed to explain how the de-excitation process has been simulated.

In light of the high decay rate of the 6P state, we can describe the target Rydberg evolution using rate equations [34] as follows:

$$\frac{dN_{\text{target}}}{dt} = \sum_{n'=5}^{n_{\text{max}}} \sum_{l'=l-1}^{l+1} \sum_{j'=\frac{l'-1}{2}}^{\frac{l'+1}{2}} \left( \Gamma_{n'l'j' \rightarrow nlj}^{\text{TOT}} N_{n'l'j'}(t) - \Gamma_{nlj \rightarrow n'l'j'}^{\text{TOT}} N_{\text{target}}(t) \right) - \Gamma_{\text{Dep}} N_{\text{target}} \quad (4.7)$$

Here the notation is the same as in (4.3) and  $\Gamma_{\text{Dep}}$  is the de-excitation rate. Considering that  $\Gamma_{\text{Dep}} \gg \sum_{n'l's'} \Gamma_{nlj \rightarrow n'l'j'}^{\text{TOT}}$ , for the purpose of calculating the depump rate, we can approximate equation (4.7) with:

$$\frac{dN_{\text{target}}}{dt} = -\Gamma_{\text{Dep}} N_{\text{target}} \rightarrow N_{\text{target}}(t) = N_0 e^{-\Gamma_{\text{Dep}} t} \quad (4.8)$$

imposing that after 10 microseconds the population in that state is decreased by a factor  $1 - \xi_{\text{Dep}}$ , i.e. a depump efficiency of  $\xi_{\text{Dep}}$ , we can calculate the rate as:

$$\Gamma_{\text{Dep}} = -\frac{1}{10} \log(1 - \xi_{\text{Dep}}) \quad [\text{kHz}] \quad (4.9)$$

It is important to observe the values of  $\Gamma_{\text{Dep}}$  for different depump efficiency:

Eff <sub>Dep</sub> [%]	$\Gamma_{\text{Dep}}$ [MHz]
50	0.07
60	0.09
70	0.12
80	0.16
90	0.23

Since those values are much lower than the inverse of the time step used in the previous simulations  $\frac{1}{t_{\text{step}}} = 20 \text{ MHz}$ , choosing as above  $t_{\text{step}} = 50 \text{ ns}$  the concept of transition proba-

bility (4.5) is still valid.

To implement this process in the simulation I have created a scheme similar to what we do in our experiments. Two independent lists are created. The first follows the same evolution as previously explained without any change. From that the ensemble population is counted and, to monitor the effective depump efficiency, also the target population is counted.

The evolution of the second list differs from the first one only during 10 microseconds before counting. In this time interval the evolution is controlled by a new function called `Depump(STATO *s, double DepRate)` in which the value of  $\Gamma_{Dep}$ , calculated from (4.9), is added to the decay rate  $\Gamma_{Gnd}$ .

From this second list the total number of atoms that remain in the list is extracted, representing the support population as defined in the previous chapter.

The number of atoms in the target state is computed by subtracting the support calculation from the ensemble one. An example of the calculated populations compared to experimental data is shown in Fig(4.4). In this figure I also show the relative difference between the lifetime calculated with the previous method and the lifetime calculated with the new depump procedure  $100 * \frac{\tau_{previous} - \tau(Dep)}{\tau_{previous}}$ , for various de-excitation efficiencies.

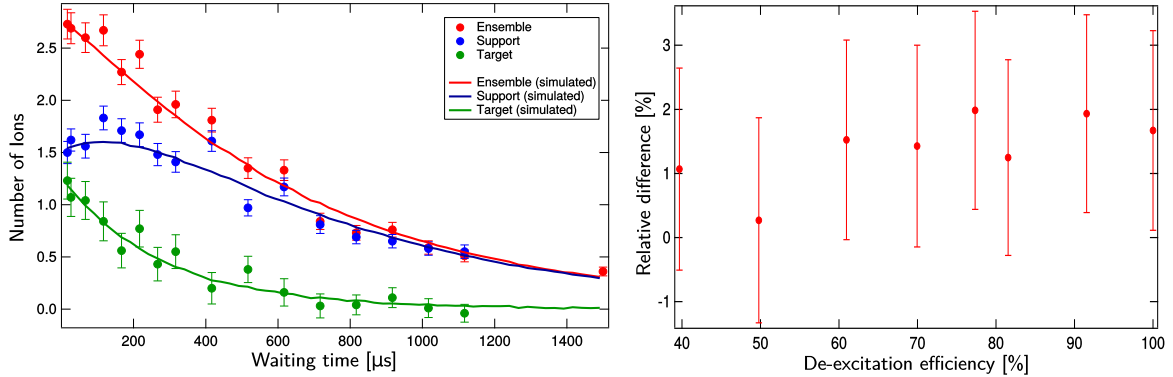


Figure 4.4: (a) Simulation of 60% inefficient de-excitation measurement for  $|80P_{3/2}\rangle$  state. The red line shows the ensemble data extracted from the first list, the blue line represents the support data extracted from the second list in which the de-excitation is simulated. The green line represents the difference of the two measurement. Finally the dots are the experimental data with the same colour definition.(b) Plot of the relative difference of simulated data with and without de-excitation technique as a function of de-excitation efficiency for the state  $|85P_{3/2}\rangle$ .

The difference between the two calculated lifetimes is about 1%. This fact shows that our measurement could be slightly underestimated by few percent but, at the same time, that the depressions of more than 50% seen in the ranges from 90 to 100 is not due to the

inefficient de-excitation technique. As an expected result we can see that increasing the depump efficiency has no effects on the calculated lifetime.

### 4.3 Comparison with theoretical predictions in literature

In this final section I want to expose a comparison of the data obtained using ARC calculation and theoretical results found in the literature.

At first, I compare the lifetimes for various S states at  $T = 0$  and at  $T \neq 0$  without repopulation, calculated with ARC, and the results obtained by I.I.Beterov [23] Tab(4.2). These two calculations do not depend on the method used to simulate the evolution of the states, but only on the sum of all the transition rates calculated from (4.2). The difference between those results could be due to different methods used to evaluate integrals, or approximations used to compute the Rydberg wavefunctions.

$nS$	Lifetimes without repopulation [ $\mu s$ ]					
	$T = 0K$			$T = 300K$		
	$\tau_{Bet}$	$\tau_{ARC}$	Diff[%]	$\tau_{Bet}$	$\tau_{ARC}$	Diff[%]
55	191	175	8.3	83	80	3.6
60	252	230	8.7	104	100	4
65	325	297	8.6	126	122	3.2
70	410	375	8.5	152	147	3.3
75	509	465	8.6	179	174	2.8
80	624	569	8.8	209	204	2.4

Table 4.2: Comparison of  $T = 0K$  and  $T = 300K$  lifetimes for various Rydberg states. The first results are calculated by I.I.Beterov in [23] while the second using the built-in function of ARC `atom.getStateLifetime()`. The two relative differences are calculated as  $Diff = 100 \frac{\tau_{Bet} - \tau_{ARC}}{\tau_{Bet}}$ . Significant differences appear in the results at  $T = 0 K$  whereas the differences for  $T = 300 K$  are significantly smaller.

The ARC lifetimes at  $T = 0K$  are somewhat lower than expected from those reported by Beterov. This may be due to the program ARC overestimating the decay rates. Moreover the BBR transition rates calculated by ARC are overestimated with respect to I.I.Beterov calculations, in fact the lifetimes at  $T = 300K$  have significantly lower relative differences. Using ARC to calculate the transition rates, the results obtained with my program will deviate by a few percent from those reported by I.I.Beterov, but, if the discrepancies remain below typical experimental error of  $\sim 10\%$ , we can consider my results as a good reference to confront experimental values with.

For the simulations of S states I used the same parameters used in P states calculations. In

Tab(4.3) the relative differences from my simulated data and those of Beterov are reported, the errors on my simulated data are less than 0.1%.

As expected, the discrepancies in target lifetimes are few percent larger than the ones in the previous table, whereas, unexpectedly, the calculated ensemble lifetimes are slightly higher than Beterov's values. In general, the discrepancies are lower than typical experimental errors.

$nS$	Lifetimes with repopulation [ $\mu s$ ]					
	Target			Ensemble		
	$\tau_{\text{Bet}}$	$\tau_{\text{Me}}$	Diff[%]	$\tau_{\text{Bet}}$	$\tau_{\text{Me}}$	Diff[%]
70	168	154	8.3	389	406	-4.4
75	196	183	6.6	482	506	-5.0
77	207	195	5.8	523	548	-4.7
80	226	212	6.2	590	609	-3.2
82	238	228	4.2	642	662	-3.0
85	258	253	2.3	693	651	-6.1
86	264	255	3.4	746	760	-1.8
90	293	286	2.4	860	872	-1.4
93	315	310	1.9	953	961	-0.8
94	323	318	1.5	985	993	-0.8
95	331	326	1.5	1019	1024	-0.5

Table 4.3: Comparison of data simulated using my program with data calculated by I.I.Beterov in [33]. The first three columns refer to target lifetimes and the second ones refer to ensemble lifetime. The relative difference is calculated as in the previous table.

## 4.4 Conclusion

This chapter had the aim of presenting the program realised to calculate the lifetimes of Rydberg atoms for S and P states. With this program I have produced a set of theoretical values for P states that is a better reference than calculation realised using only ARC built-in functions.

Moreover, the excitation of a population in a P state and in the nearest S state was investigated, confirming that this process cannot be responsible for the depressions seen in experimental data. Finally the inefficient de-excitation protocol used to measure the P states lifetime was checked, observing whether it can alter the measured data or not. From the results obtained we can expect no deviations caused by the partial de-excitation of the target state.

## Chapter 5

# Qualitative analysis of Blackbody spectrum in our apparatus

In chapter 3 I presented our experimental results on S and P states lifetime. For S states we observe a good agreement with theoretical predictions except for two small ranges of principal quantum numbers, whereas, for P states, we observe a general more scattered behaviour but clearly in the same ranges of principal quantum numbers similar deviations are observed.

In section 3.1 I described the conditions in which our experiments are performed, emphasising our control on the parameters that could disturb our measurements. Interactions between Rydberg atoms or with external stray electric field were excluded. Moreover, to check the presence of external microwave radiations inside the vacuum cell we shielded our apparatus with a Faraday cage (section 3.3) but no changes in the measured lifetime were observed in the deviation regions.

These considerations leave as a plausible explanation of the deviated lifetimes an alteration of the density of modes of BBR. Deviations from Planck's formula have already been predicted theoretically [35] and observed experimentally using Rydberg atoms [36]. In [36] they utilise a millimeter-sized cavity with tunable dimensions. They observed that when the cavity size is tuned to the wavelength of a first neighbour Rydberg transition, the BBR induced transition rate to neighboring state is enhanced significantly.

In our apparatus we do not have a cavity, but, since the transition wavelengths involved in our experiments are on the order of few centimeters, the combination of various objects close the vacuum cell or the vacuum cell itself can create an effective cavity for microwave radiation.

Unfortunately to verify such a hypothesis directly we would have to change the disposition of the objects close to the vacuum cell but, at the moment, this is unfeasible. However a pos-

sible confirmation could be achieved in collaboration with other groups which use a different set-up. If this hypothesis is right, measuring the lifetime with our protocol but with different physical environment must lead to similar deviations in different frequency ranges.

In the following sections I will introduce a simple model to characterise qualitatively the effective density of modes of the electromagnetic field from the measured lifetimes. A Python algorithm was developed to find an optimal set of parameters given a model function. After that I used the hypothesis of [37] to develop a toy model that reproduces a similar spectrum.

## 5.1 Simple model for the expected deviation

Looking at the experimental results exposed in chapter 3, it appears that the two ranges,  $4 \div 5$  GHz and  $9 \div 11$  GHz, are principally altered. A qualitative description of the deviation can be made, in principle, using lorentzian functions, the typical mode distributions in a cavity. I defined the deviation function  $D(\nu, \{\beta\})$  as:

$$D(\nu, \{\beta\}) = \frac{\rho_{\text{Model}}(\nu, \{\beta\})}{\rho_{\text{Inf}}(\nu)} = 1 + a_1 \frac{\Delta\nu_1}{(\nu - \nu_1)^2 + \Delta\nu_1^2} + a_2 \frac{\Delta\nu_2}{(\nu - \nu_2)^2 + \Delta\nu_2^2} \quad (5.1)$$

where  $\rho_{\text{Inf}}(\nu)$  is the density of mode calculated in the infinite sized box approximation (1.14) and the set of coefficients  $\beta = \{a_1, a_2, \nu_1, \nu_2, \Delta\nu_1, \Delta\nu_2\}$  will be adjusted with a minimisation routine.

Each blackbody transition rate (1.6) is linear with the density of modes at the correspondent transition frequency. Using this model, each BBR induced rate has to be modified with the deviation function, leading to a total BBR transition rate:

$$\Gamma_{nlj}^{(\text{Model})} = \sum_{n'l'j'} \Gamma_{nlj \rightarrow n'l'j'}^{(\text{BBR})} D(\nu_{nlj \rightarrow n'l'j'}, \{\beta\}) \quad (5.2)$$

The spontaneous emission rate can be considered unperturbed, because, as shown in Fig(4.1), it is significant only for small wavelength transitions, on the order of few hundreds of nanometers, which we assume to be unaltered by the environment.

The lifetime of Rydberg atoms is calculated replacing  $\Gamma_{nlj}^{(\text{BBR})}$  with (5.2).

$$\tau_{nlj}(\beta_j) = \left( \Gamma_{nlj}^{\text{Spon}} + \Gamma_{nlj}^{\text{Model}}(\beta_j) \right)^{-1} \quad (5.3)$$

For the calculation which I will explain below, the program used in the previous chapter is not suitable. Instead I used the function `atom.getTransitionRate()` of the ARC library.

To include the effect of repopulation the calculated lifetime is increased by 6.5%, which is the averaged relative difference of Tab(4.1). Using this procedure we have the lifetime of a specific Rydberg state as a function of the set of coefficients  $\beta_j$ . We cannot use a standard fit method to derive the best set of parameters because of the large number of parameters involved. This problem is addressed using an iterative search of the minimum value of the squared residual.

I use as initial values for the centre of the lorentzian functions the first neighbouring transition frequencies for the 72S and the 92S and as heights the fractions  $a_1^{in} = \tau_{72S}^{theo} / \tau_{72S}^{exp}$  and  $a_2^{in} = \tau_{92S}^{theo} / \tau_{92S}^{exp}$ . For the widths I use initial values in such a way that each frequency of Tab(3.1) has slightly increased density of modes. For each coefficient I defined an acceptable range respectively:  $[0, 2a_1^{in}]$ ,  $[0, 2a_2^{in}]$ ,  $[0.5w_1^{in}, 1.5w_1^{in}]$ ,  $[0.5w_2^{in}, 1.5w_2^{in}]$ ,  $[0, 2dw_1^{in}]$ ,  $[0, 2dw_2^{in}]$ .

The smaller ranges for the centre of the lorentzian is chosen in order not to overlap the two peaks. Given a set of coefficients, each Rydberg state lifetime is computed and the squared residual is evaluated as:

$$Res_j = \sum_i \left( \frac{\tau_i^{Model}(\beta_j) - \tau_i^{Exp}}{\Delta\tau_i} \right)^2 \quad (5.4)$$

In this calculation both P and S states are included.

After that a single parameter, chosen at random, is varied inside the acceptable range and the residual value corresponding to the new set of parameters is calculated. Each time the function finds a new smaller residual value, it is recorded with the respective set of parameters. The program is stopped after  $10^7$  different combinations of coefficients and returns the last set of parameters  $\beta$  recorded. This procedure is repeated ten times, with various initial values. The returned sets of minimum parameters differs less than 10% from each other. The best agreement with theoretical data is found with the set:  $\beta_{MIN} = \{a_1 = 2.66, a_2 = 0.87, \nu_1 = 4.64 \text{ GHz}, \nu_2 = 11.2 \text{ GHz}, \Delta\nu_1 = 0.49 \text{ GHz}, \Delta\nu = 0.31 \text{ GHz}\}$ , the results are shown in Fig.(5.1).

From these results we can understand that a model with only two peaks is too simple to describe our data. In fact, as mentioned in chapter 3, other deviations around 3 GHz are predicted. Changing  $D(\nu)$  to a three lorentzian peaks function and repeating the same analysis we found in fact better agreement as shown in Fig(5.2) with the peaks centred at 2.54 GHz, 4.6 GHz, and 11.02 GHz.

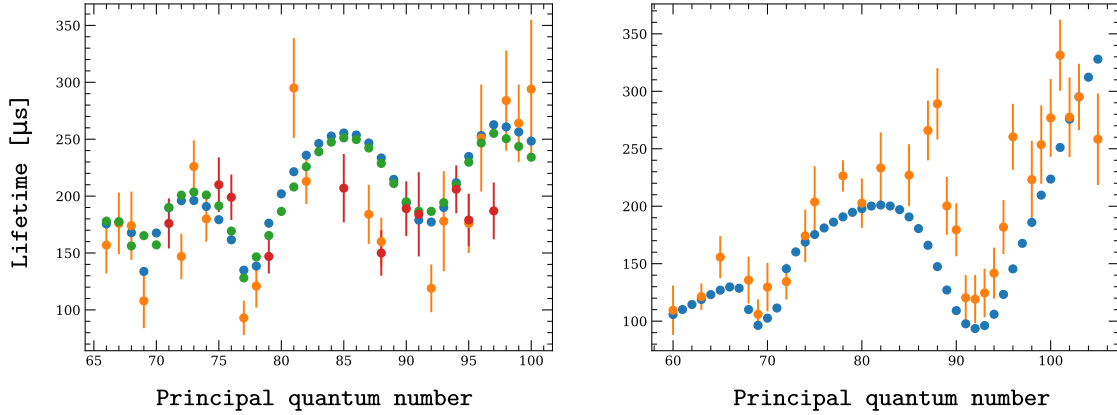


Figure 5.1: Experimental results and calculated lifetimes for P (**left**) and S (**right**) states. In the plot on the left, the orange and red dots represent respectively the experimental data for  $J = 3/2$  states and  $J = 1/2$  states, whereas the blue and green dots represent calculated values for  $J = 3/2$  states and  $J = 1/2$  states. The blackbody spectrum which minimizes the square residual is:  $u_{\nu}^{\text{Model}} = u_{\nu}^{\text{Planck}} D(\nu, \beta_{\text{MIN}})$  where  $D(\nu, \beta_{\text{MIN}})$

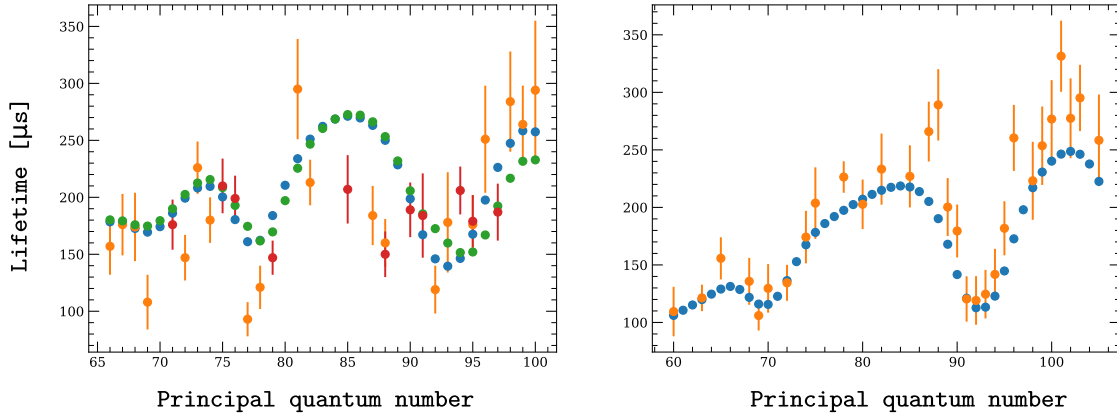


Figure 5.2: Experimental results and calculated lifetimes for P (**left**) and S (**right**) states. In the plot on the left, the orange and red dots represent respectively the experimental data for  $J = 3/2$  states and  $J = 1/2$  states, whereas the blue and green dots represent calculated values for  $J = 3/2$  states and  $J = 1/2$  states. The minimization was performed with a three Lorentzian function.

For this optimization algorithm I cannot use the program exposed in the previous chapter because, for a single set of coefficients, lifetimes for each of the measured states have to be evaluated. My program takes about an hour for a single lifetime calculation so about three

days to check a given set of coefficients.

From this discussion we can understand that a simple three peaks model for the deviation of density of modes agree only qualitatively with experimental data. Nevertheless the developed method to evaluate the coefficients of a deviation function is an efficient method and it can be used to test more elaborate models of the spectral density.

## 5.2 Toy model for the calculation of the blackbody spectrum

In this section I develop a simple toy model based on the geometry of our apparatus. As already emphasised I am not looking for a quantitative agreement with experimental data because, in the condition exposed, each object nearby the cell must be taken into account as a blackbody emitter. Fig.(5.3) shows a photo of the vacuum cell and the surrounding apparatus.

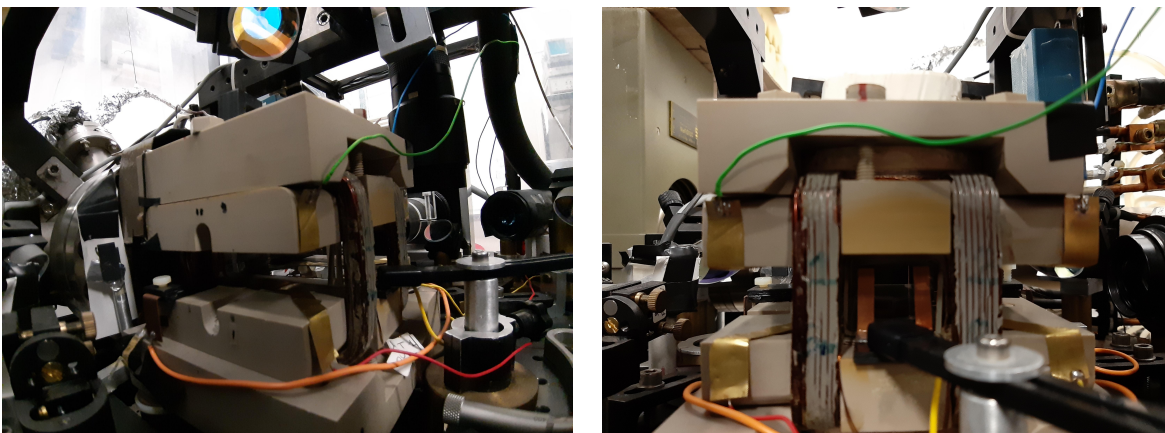


Figure 5.3: Frontal and lateral views of the vacuum cell and the experimental set-up close to it.

The first emitter considered is obviously the quartz cell itself with external dimensions:  $3 \times 2.4 \times 9$  cm, and internal dimensions:  $1.8 \times 2.4 \times 9$  cm. Actually the longest dimension is not well-defined because the face near the channeltron is absent to connect the cell to the vacuum system.

Although quartz has a low reflection coefficient in the microwave region [38], in our apparatus the adsorbed Rubidium has created a thin metallic layer that, we suppose, has significantly increased the reflection coefficient.

As shown L.Di Virgilio's thesis [12] the electric field created by the external electrodes and measured at the MOT position is around 10 times smaller than theoretically expected. This

large reduction of the electric field cannot be explained only with dielectric properties of the quartz and a possible explanation lies in such a layer of metallic Rubidium on the internal surfaces of the vacuum cell.

Assuming a closed cavity of length  $L$  and a reflectivity  $\mathcal{R}$ , the lifetime of a photon inside that cavity can be calculated as [39]:

$$\tau_P = \frac{2L}{c} \frac{1}{\log(\mathcal{R}^2)} \quad (5.5)$$

This lifetime leads to a Lorentzian frequency distribution of width  $\Delta\nu = (2\pi\tau_P)^{-1}$  for each resonant mode:

$$E_n(\nu) = \frac{1}{\pi} \frac{\Delta\nu}{(\nu - \nu_n)^2 + \Delta\nu^2} \quad (5.6)$$

To evaluate the density of modes inside the cavity we can sum all the resonant modes with their distribution divided by the volume of the cavity. From this quantity we can derive the deviation function defined in the previous section (5.1).

For the calculations I used a simple model in which the cavity is considered closed and hence with dimensions  $1.8 \times 2.4 \times 9$  cm. The deviation functions for various reflectivities are shown in Fig.(5.4).

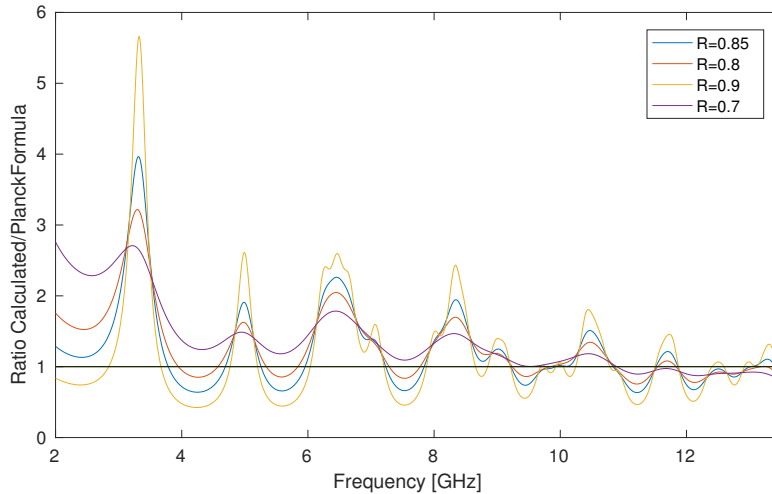


Figure 5.4: Simulation of the blackbody spectrum emitted by a closed cavity of dimensions  $2.4 \times 1.8 \times 9$  cm. The lines represent the ratio between the density of modes of such a cavity and the density of modes of free space for various reflectivities.

From this extremely simple model we can see that the possible deviations are on the entire spectral range from 2 to 14 GHz. Finally, as a last consideration I want to underline the fact

that inside the cavity the electromagnetic field forms standing waves which implies inhomogeneous energy distribution. Consequently only the waves with antinodes at the MOT position (which is roughly at the symmetry centre of the cross-section of the cell) are effectively felt by the atoms.

### 5.3 Conclusion

In this chapter a qualitative discussion of the deviation from theoretical predictions, seen in the experimental data, was presented.

I developed a method to estimate the coefficients of a deviation function  $D(\nu)$  from the experimental data by means of an optimisation protocol. The method was tested with two simple functions, composed of two or three lorentzian enhancements, obtaining qualitative agreement in spite of the simplicity of the model. The study of more detailed functions for such a deviation is left as an outlook.

Finally, I described the toy model for the density of modes inside the cavity. The results obtained give us a first insight into the complex behaviour of the spectral density we can expect for our apparatus.

# Chapter 6

## Conclusion

This thesis reports experimental studies of the lifetime of S, P and D high-lying Rydberg states used to characterise blackbody induced transitions.

I have shown the techniques exploited to excite and selectively de-excite single Rydberg states with different angular momenta. I have demonstrated that using these techniques and controlling the experimental conditions to avoid state mixing we are able to accurately measure the individual and ensemble lifetimes of high-lying S, P and D Rydberg states.

Numerical simulations of the dynamics of a Rydberg state interacting with blackbody radiation have been performed to produce theoretical predictions that take into account repopulation processes.

The results for S states have shown that in two regions of principal quantum numbers the measured lifetime is significantly lower than expected.

The results for P states have confirmed such lower lifetimes in the same regions of principal quantum number, but, a new deviation from theoretical prediction appears.

With an analysis of the first neighbouring transition frequencies for the states in those ranges of principal quantum numbers I have highlighted a correlation between measured lifetimes that are shorter than expected and the corresponding transition frequencies.

The D state lifetimes are currently under investigation but, from the preliminary, a similar behaviour is observed.

From the experimental conditions presented in chapter 3, and the results obtained with the shielding cage we can exclude that the lower measured lifetimes are caused by interactions, uncompensated electric fields or by the presence of external signals.

Up to now the most plausible explanation for such deviations is an alteration of Planck's formula caused by the geometry of our apparatus.

The first transition wavelengths of the states we have investigated in our experiments are of

the order of few centimeters, such as the geometrical size of various objects nearby the MOT. Furthermore I developed a Python program to analyse the experimental data in terms of deviated density of modes, highlighting that a deviation function composed of just three peaks fit only qualitatively the data.

From the calculation of the blackbody spectrum emitted by a cavity of the same dimensions as our vacuum cell I demonstrated that various frequencies could have enhanced or decreased density of modes.

Finally, I also pointed out that for a complete understanding of the electromagnetic spectrum at the MOT position we must consider that inside a partially reflecting object the intensity of each mode becomes space dependent.

A more detailed analysis of this behaviour is beyond the purposes of this thesis and is left as an outlook.

## Appendix A

# Calculation of the three-photon Rabi frequency

Using three different electromagnetic waves to couple our ground state to the excited P Rydberg state, we can write the Hamiltonian of the atom as:

$$H = H_0 + \frac{1}{2} \hat{d} \cdot \left[ \mathbf{E}_B (e^{i2\pi\nu_B t} + e^{-i2\pi\nu_B t}) + \mathbf{E}_{IR} (e^{i2\pi\nu_{IR} t} + e^{-i2\pi\nu_{IR} t}) + \mathbf{E}_{MW} (e^{i2\pi\nu_{MW} t} + e^{-i2\pi\nu_{MW} t}) \right] \quad (\text{A.1})$$

where  $\nu_B = \frac{E_{6P_{3/2}} - E_{5S_{1/2}}}{h} + \delta_B$ , is the frequency of the blue laser,  $\nu_{IR} = \frac{E_{nRy} - E_{6P_{3/2}}}{h} + \delta_{IR} - \delta_{Blue}$  is the frequency of the infrared laser and finally  $\nu_{MW} = \frac{E_{nRyP} - E_{n'RyP}}{h} - \delta_{IR}$ . The spatial dependence of the waves will be considered constant in the following discussion.

From time dependent perturbation theory we can calculate the amplitude of a certain transition solving:

$$\dot{a}_k(t) = -\frac{1}{\hbar} \sum_s \tilde{V}_{ks}(t) a_s(t) \quad (\text{A.2})$$

here I used the interaction representation for the potential  $\tilde{V}_{ks}(t) = e^{i\epsilon_k t/\hbar} V_{ks}(t) e^{-i\epsilon_s t/\hbar}$ .

At the first perturbative order only the blue laser can couple with the ground state, and the amplitude of the intermediate  $|6P_{3/2}\rangle$  can be calculated as:

$$a_{6P}^{(1)} = \Omega_B \left[ \frac{1 - e^{-i2\pi(\nu_{6P,5S} - \nu_B)t}}{2\pi(\nu_{6P,5S} - \nu_B)} \right] = \Omega_B \left[ \frac{1 - e^{-i2\pi(\delta_B)t}}{2\pi\delta_B} \right] \quad (\text{A.3})$$

For which we define the one-photon Rabi frequency as  $\Omega_B = \frac{1}{\hbar} \langle 6P_{3/2} | \hat{d} | 5S_{1/2} \rangle \cdot \mathbf{E}_B$  and the transition frequency  $\nu_{i,j} = \frac{E_i - E_j}{h}$ . All the other possible transition can be neglected because strongly non-resonant.

We can now calculate the second order perturbative amplitude inserting (A.3) in (A.2) ob-

serving that only the infrared photon is not strongly out of resonance:

$$a_{nRyS}^{(2)} = \frac{\Omega_B \Omega_{IR}}{2\pi\delta_B} \left[ \frac{1 - e^{-i2\pi(\delta_{IR})t}}{2\pi\delta_{IR}} \right] \quad (\text{A.4})$$

As above I defied the single photon Rabi frequency for the second step as  $\Omega_{IR} = \frac{1}{\hbar} \langle nRyS | \hat{d} | 6P_{3/2} \rangle \cdot \mathbf{E}_{IR}$ . Repeating the same steps we can calculate the three-photon amplitude of the P Rydberg state (neglecting again all the non-resonant photons) as:

$$a_{nRyP}^{(3)} = \frac{\Omega_B \Omega_{IR} \Omega_{MW}}{(2\pi)^2 \delta_B \delta_{IR}} \left[ \frac{1 - e^{-i2\pi(\nu_{nRyP,5S} - \nu_B - \nu_{IR} - \nu_{MW})t}}{2\pi(\nu_{nRyP,5S} - \nu_B - \nu_{IR} - \nu_{MW})} \right] \quad (\text{A.5})$$

Once the electromagnetic waves are switched off, the probability of exciting the desired state, using the same derivation of Fermi golden rule, is:

$$P_{nRyP} = 2\pi \left| \frac{\Omega_B \Omega_{IR} \Omega_{MW}}{(2\pi)^2 \delta_B \delta_{IR}} \right|^2 \rho(\nu_{nRyP,5S} - \nu_B - \nu_{IR} - \nu_{MW}) \quad (\text{A.6})$$

Where  $\rho(\nu)$  is the frequency width of the transition, in which are considered the natural width of the atom, the Doppler broadening and the lasers linewidth. From this formula we can define the three-photon Rabi frequency as:

$$\Omega_{3-photon} = \frac{\Omega_B \Omega_{IR} \Omega_{MW}}{(2\pi)^2 \delta_B \delta_{IR}} \quad (\text{A.7})$$

# Appendix B

## Lifetime program

This part of the appendix is dedicated to the description of the basics of the lifetime program presented in chapter 4. In particular I will describe in detail the construction of the structure `STATE` and the evolution functions.

### B.1 Definition of the structure `STATE`

As already exposed in chapter 4 the structure `STATE` contains the properties of a given quantum state, necessary to simulate its evolution: the three quantum number of the state  $n, l, j$  and the list of all the relevant transition rates (BBR induced and spontaneous decay). In C language this structure is written as follows:

```
typedef struct state
{
  int E;
  int L;
  double J;

  struct rate*;
}STATE
```

Here `rate*` is a pointer to another structure `RATE`. The structure `RATE` is composed by a double `r` and a pointer to a structure `STATE *s`:

```
typedef struct rate
{
double r;
STATE *s;
}RATE
```

here  $r$  is the total transition rate from the state  $n l j$  to the state  $n' l' j'$  ( $\Gamma_{nlj \rightarrow n'l'j'}^{TOT}$ ), as defined in equation (4.3), expressed in Hz and  $*s$  is the memory address of the arrival state. Using ARC I defined all the structure in the range of principal quantum numbers taken into account ( $59 < n < 100$ ). All the states with principal quantum number lower than 59 are considered as a unique ground state  $s5\_0\_0$  and the rate to this state is  $\Gamma_{nlj}^{GND} = \sum_{n' < 59} \sum_{l', j'} \Gamma_{nlj \rightarrow n'l'j'}^{TOT}$ . An example of the definition of such a structure is:

```
STATE s95_0_0 ={ 95 , 0 , 0.5,
    1087.79, &s5_0_0,
    1.62, &s60_1_1,
    0.91, &s60_1_0,
    .
    .
    .
    496.66, &s94_1_1,
    252.23, &s94_1_0,
    .
    .
    .
    1.81, &s110_1_1,
    0.77, &s110_1_0,
}
```

Here I have reported only seven transitions to do not annoy the reader.

With this kind of structure each state is linked to all the states with angular momentum that differs of  $\pm 1$  and to the ground state forming a network of states.

A simplified scheme of such a network is shown in Fig(B.1), in which only 3 states for each angular momentum are depicted.

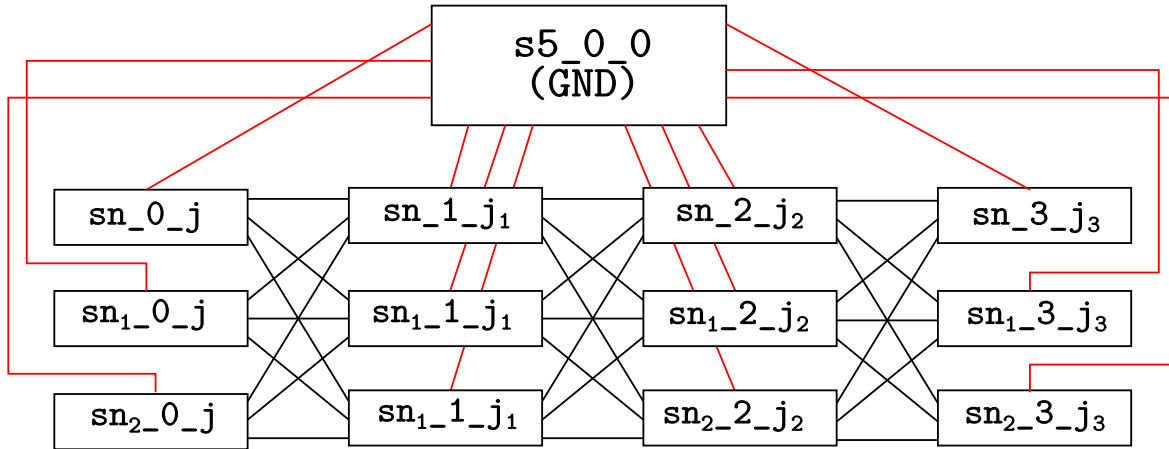


Figure B.1: Simplified scheme of the network implemented in the simulation.

At the beginning of the program the three quantum numbers of the state we want to excite and the number of initial state ( $N_{exc}$ ) are required.  $N_{exc}$  pointers that point to the selected state are created and inserted in a list defined as:

```
typedef struct list
{
STATE *s;
struct list *next;
}LIST
```

## B.2 Evolution of a state

Once the list of states is created the evolution of each state is performed by the function `evolve( STATE *s )` which receives as input a pointer to the STATE `s`. This function is written as follows:

```
STATE *evolve(STATE *s)
{
RATE *arr=(s->r);
//arr is a pointer to the first structure rate present in the structure STATE s

int n=len(s);
// len(STATE *s) is a function that calculate
//how many allowed transitions are present in the structure s
```

```

    double r;
    r=genrand_real1()/(tstep);
//genrand_real1 generates the random number 0<r<1
    while(r>=0)
    {
        if(n<0)
            return s;
        n--;
        r-=(arr[n].r);
    }
    return arr[n].s;
}

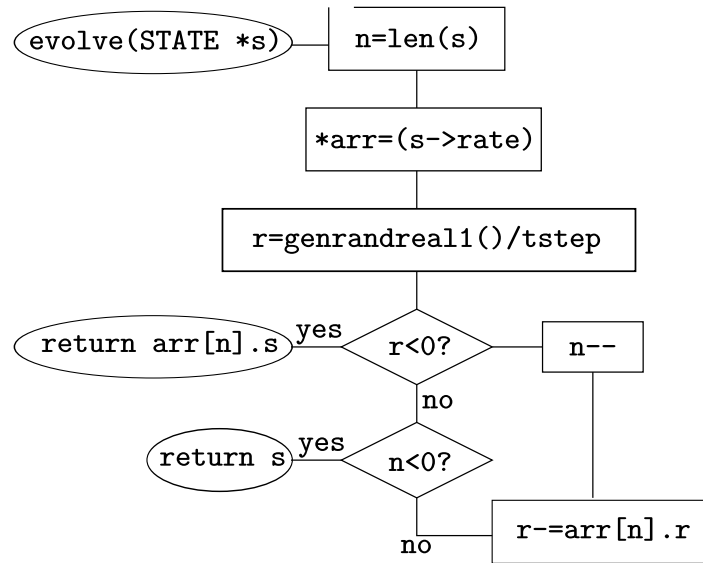
```

In this function a pointer that point to the first structure `RATE` of the `STATE s` is created and is calculated how many allowed transitions are present is such a `STATE`.

The number of allowed transitions is different for different angular momenta, for example: an S state can transit only to P state whereas a P state has allowed transitions to S and D states. After that a random number  $0 < r < 1$  is generated using a *Marsenne-Twister* algorithm [40] that is by far the most widely used pseudo-random number generator.

Each rate in the structure `STATE` has to be scaled by a factor `tstep` to become a transition probability, as defined in ( ref prob). This procedure is highly inefficient because lots of operations have to be performed to convert all the rates of a single `STATE`. A more clever procedure is to scale the probability range  $[0, 1]$  to  $[0, 1/tstep]$ .

At this point, a while cycle, which stops if  $r < 0$ , starts. In the  $n$ th loop of this cycle the rate of the  $n$ th transition in the structure is subtracted from `r`. If `r` is greater than zero after subtracting all the transition rates, no transition occurs and the pointer `*s` still point `sn.l-j`. On the contrary if subtracting a certain rate, for example `r_n111j1`, the random number `r` become negative, the cycle stops and the pointer `*s` points to `sn1.l1_j1`. After the call of this function the input `STATE` is updated with the `STATE` returned. To a better understanding of the function `evolve( STATE *s)`, Fig(B.2) shows the block diagram of such a function.

Figure B.2: Block diagram of the function `evolve( STATE *s)`

To evolve each state present in the list and to clean the list from the states decayed in the "ground" state I create the function `event(LIST **p)` which has the following syntax:

```

void event(LIST **p)
{
    STATE *s;
    while((*p)!=NULL)
    {
        f=evolve((*p)->s);
        if (f->E==5) \\cleaning of the ground state
            clean(p);
        else
        {
            (*p)->s=f;
            p=&(**p).next;
        }
    }
}

```

# Bibliography

- [1] R. P. Feynman, “Simulating physics with computers,” *International journal of theoretical physics*, vol. 21, no. 6, pp. 467–488, 1982.
- [2] H. Weimer, M. Müller, I. Lesanovsky, P. Zoller, and H. P. Büchler, “A Rydberg quantum simulator,” *Nature Physics*, vol. 6, no. 5, p. 382, 2010.
- [3] M. M. Valado, C. Simonelli, M. D. Hoogerland, I. Lesanovsky, J. P. Garrahan, E. Arimondo, D. Ciampini, and O. Morsch, “Experimental observation of controllable kinetic constraints in a cold atomic gas,” *Physical Review A*, vol. 93, no. 4, p. 040 701, 2016.
- [4] T. F. Gallagher and W. E. Cooke, “Interactions of blackbody radiation with atoms,” *Physical Review Letters*, vol. 42, no. 13, p. 835, 1979.
- [5] T. F. Gallagher, *Rydberg atoms*. Cambridge University Press, 2005, vol. 3.
- [6] D. B. Branden, T. Juhasz, T. Mahlokozera, C. Vesa, R. O. Wilson, M. Zheng, A. Korytna, and D. A. Tate, “Radiative lifetime measurements of rubidium Rydberg states,” *Journal of Physics B: atomic, molecular and optical physics*, vol. 43, no. 1, p. 015 002, 2009.
- [7] L. G. Marcassa, “Measurement of Rydberg state lifetimes using cold trapped neutral atoms,” *Physica Scripta*, vol. 2009, no. T134, p. 014 011, 2009.
- [8] M. Mack, J. Grimm, F. Karlewski, L. Sárkány, H. Hattermann, and J. Fortágh, “All-optical measurement of Rydberg-state lifetimes,” *Physical Review A*, vol. 92, no. 1, p. 012 517, 2015.
- [9] M. Archimi, C. Simonelli, L. Di Virgilio, A. Greco, M. Ceccanti, E. Arimondo, D. Ciampini, I. I. Ryabtsev, I. I. Beterov, and O. Morsch, “Measurements of individual and ensemble lifetimes of high-lying Rb Rydberg states,” *arXiv e-prints*, arXiv:1907.01254, 2019.

- [10] M. Archimi, “Experimental studies of the blackbody induced population migration in dissipative Rydberg systems,” PhD Thesis, Università di Pisa, 2019.
- [11] A. Greco, “Experimental studies of the lifetimes of rubidium Rydberg atoms as sensors of blackbody radiation,” Master Thesis, Università di Pisa, 2019.
- [12] L. Di Virgilio, “Characterization and compensation of stray electric fields in cold Rydberg atoms experiments,” Master Thesis, Università di Pisa, 2019.
- [13] W. Li, I. Mourachko, M. W. Noel, and T. F. Gallagher, “Millimeter-wave spectroscopy of cold Rb Rydberg atoms in a magneto-optical trap: Quantum defects of the ns, np, and nd series,” *Physical Review A*, vol. 67, no. 5, p. 052 502, 2003.
- [14] R. Löw, H. Weimer, J. Nipper, J. B. Balewski, B. Butscher, H. P. Büchler, and T. Pfau, “An experimental and theoretical guide to strongly interacting Rydberg gases,” *Journal of Physics B: Atomic, Molecular and Optical Physics*, vol. 45, no. 11, p. 113 001, 2012.
- [15] W. P. Spencer, A. G. Vaidyanathan, D. Kleppner, and T. W. Ducas, “Temperature dependence of blackbody-radiation-induced transfer among highly excited states of sodium,” *Physical Review A*, vol. 25, no. 1, p. 380, 1982.
- [16] N. Šibalić, J. D. Pritchard, C. S. Adams, and K. J. Weatherill, “ARC: An open-source library for calculating properties of alkali Rydberg atoms,” *Computer Physics Communications*, vol. 220, pp. 319–331, 2017.
- [17] S. Haroche and D. Kleppner, “Cavity quantum electrodynamics,” *Phys. Today*, vol. 42, no. 1, pp. 24–30, 1989.
- [18] R. G. Hulet, E. S. Hilfer, and D. Kleppner, “Inhibited spontaneous emission by a Rydberg atom,” *Physical review letters*, vol. 55, no. 20, p. 2137, 1985.
- [19] P. H. Goy, J. M. Raimond, M. Gross, and S. Haroche, “Observation of cavity-enhanced single-atom spontaneous emission,” *Physical Review Letters*, vol. 50, no. 24, p. 1903, 1983.
- [20] K. Konishi and G. Paffuti, *Quantum mechanics: a new introduction*. OUP Oxford, 2009.
- [21] E. Urban, T. A. Johnson, T. Henage, L. Isenhower, D. D. Yavuz, T. G. Walker, and M. Saffman, “Observation of Rydberg blockade between two atoms,” *Nature Physics*, vol. 5, no. 2, p. 110, 2009.
- [22] C. Cohen-Tannoudji *et al.*, *Advances in atomic physics: an overview*. World Scientific, 2011.

- [23] I. I. Beterov, I. I. Ryabtsev, D. B. Tretyakov, and V. M. Entin, “Quasiclassical calculations of blackbody-radiation-induced depopulation rates and effective lifetimes of Rydberg  $n$  S,  $n$  P, and  $n$  D alkali-metal atoms with  $n \leq 80$ ,” *Physical Review A*, vol. 79, no. 5, p. 052 504, 2009.
- [24] K. Kowalski, V. Cao Long, K. Dinh Xuan, M. Głódź, B. Nguyen Huy, and J. Szonert, “Magneto-optical trap: fundamentals and realization,” *Computational Methods in Science and Technology*, no. Vol. spec. iss.(2), pp. 115–129, 2010.
- [25] M. Viteau, J. Radogostowicz, M. G. Bason, N. Malossi, D. Ciampini, O. Morsch, and E. Arimondo, “Rydberg spectroscopy of a Rb MOT in the presence of applied or ion created electric fields,” *Optics express*, vol. 19, no. 7, pp. 6007–6019, 2011.
- [26] Y. Castin, H. Wallis, and J. Dalibard, “Limit of Doppler cooling,” *JOSA B*, vol. 6, no. 11, pp. 2046–2057, 1989.
- [27] S. Haroche and F. Hartmann, “Theory of saturated-absorption line shapes,” *Physical Review A*, vol. 6, no. 4, p. 1280, 1972.
- [28] M. Archimi, “Real space measurements of the mechanical effect of the van der waals force on Rydberg atoms,” Master Thesis, Università di Pisa, 2015.
- [29] E. A. Donley, T. P. Heavner, F. Levi, M. O. Tataw, and S. R. Jefferts, “Double-pass acousto-optic modulator system,” *Review of Scientific Instruments*, vol. 76, no. 6, p. 063 112, 2005.
- [30] D. A. Tate and T. F. Gallagher, “Microwave-optical two-photon excitation of Rydberg states,” *Physical Review A*, vol. 97, no. 3, p. 033 410, 2018.
- [31] L. V. Deputatova, V. S. Filinov, D. S. Lapitsky, V. Y. Pecherkin, R. A. Syrovatka, L. M. Vasilyak, and V. I. Vladimirov, “Measurement of the charge of a single dust particle,” in *Journal of Physics: Conference Series*, IOP Publishing, vol. 653, 2015, p. 012 129.
- [32] U. Hollenstein, R. Seiler, H. Schmutz, M. Andrist, and F. Merkt, “Selective field ionization of high Rydberg states: Application to zero-kinetic-energy photoelectron spectroscopy,” *The Journal of Chemical Physics*, vol. 115, no. 12, pp. 5461–5469, 2001.
- [33] I. I. Beterov, “Private communication.”
- [34] C. Simonelli, M. Archimi, L. Asteria, D. Capecchi, G. Masella, E. Arimondo, D. Ciampini, and O. Morsch, “Deexcitation spectroscopy of strongly interacting Rydberg gases,” *Physical Review A*, vol. 96, no. 4, p. 043 411, 2017.
- [35] A. M. García-García, “Finite-size corrections to the blackbody radiation laws,” *Physical Review A*, vol. 78, no. 2, p. 023 806, 2008.

- [36] I. I. Beterov and I. I. Ryabtsev, “Induced emission from a sodium Rydberg atom in a microwave cavity,” *Journal of Experimental and Theoretical Physics Letters*, vol. 69, no. 6, pp. 448–452, 1999.
- [37] A. Reiser and L. Schächter, “Geometric effects on blackbody radiation,” *Physical Review A*, vol. 87, no. 3, p. 033801, 2013.
- [38] P. Ängskog, M. Bäckström, and B. Vallhagen, “Measurement of radio signal propagation through window panes and energy saving windows,” in *2015 IEEE International Symposium on Electromagnetic Eompatibility (EMC)*, IEEE, 2015, pp. 74–79.
- [39] G. Moruzzi, *Appunti di struttura della materia Parte II*. 2017.
- [40] M. Matsumoto and T. Nishimura, “Mersenne twister: a 623-dimensionally equidistributed uniform pseudo-random number generator,” *ACM Transactions on Modeling and Computer Simulation (TOMACS)*, vol. 8, no. 1, pp. 3–30, 1998.